



<http://www.diva-portal.org>

This is the published version of a paper published in *Journal of Geophysical Research - Space Physics*.

Citation for the original published paper (version of record):

Roth, L., Saur, J., Retherford, K D., Strobel, D F., Feldman, P D. et al. (2016)
Europa's far ultraviolet oxygen aurora from a comprehensive set of HST observations.
Journal of Geophysical Research - Space Physics, 121(3): 2143-2170
<https://doi.org/10.1002/2015JA022073>

Access to the published version may require subscription.

N.B. When citing this work, cite the original published paper.

Permanent link to this version:

<http://urn.kb.se/resolve?urn=urn:nbn:se:kth:diva-187287>

RESEARCH ARTICLE

10.1002/2015JA022073

Europa's far ultraviolet oxygen aurora from a comprehensive set of HST observations

Key Points:

- Analysis of a large set of FUV aurora images of Europa's atmosphere
- Europa's oxygen aurora is strongly influenced by the plasma environment
- New constraints on oxygen abundances in Europa's atmosphere

Correspondence to:

L. Roth,
Lorenz.roth@ee.kth.se

Citation:

Roth, L., J. Saur, K. D. Retherford, D. F. Strobel, P. D. Feldman, M. A. McGrath, J. R. Spencer, A. Blöcker, and N. Ivchenko (2016), Europa's far ultraviolet oxygen aurora from a comprehensive set of HST observations, *J. Geophys. Res. Space Physics*, 121, 2143–2170, doi:10.1002/2015JA022073.

Received 23 OCT 2015

Accepted 18 FEB 2016

Accepted article online 22 FEB 2016

Published online 15 MAR 2016

Lorenz Roth^{1,2}, Joachim Saur³, Kurt D. Retherford², Darrell F. Strobel^{4,5}, Paul D. Feldman⁵, Melissa A. McGrath^{2,6}, John R. Spencer⁷, Aljona Blöcker³, and Nickolay Ivchenko¹

¹School of Electrical Engineering, KTH Royal Institute of Technology, Stockholm, Sweden, ²Southwest Research Institute, San Antonio, Texas, USA, ³Institute of Geophysics and Meteorology, University of Cologne, Cologne, Germany, ⁴Department of Earth and Planetary Science, The Johns Hopkins University, Baltimore, Maryland, USA, ⁵Department of Physics and Astronomy, The Johns Hopkins University, Baltimore, Maryland, USA, ⁶SETI Institute, Mountain View, California, USA, ⁷Southwest Research Institute, Boulder, Colorado, USA

Abstract We analyze a large set of far ultraviolet oxygen aurora images of Europa's atmosphere taken by Hubble's Space Telescope Imaging Spectrograph (HST/STIS) in 1999 and on 19 occasions between 2012 and 2015. We find that both brightness and aurora morphology undergo systematic variations correlated to the periodically changing plasma environment. The time variable morphology seems to be strongly affected by Europa's interaction with the magnetospheric plasma. The brightest emissions are often found in the polar region where the ambient Jovian magnetic field line is normal to Europa's disk. Near the equator, where bright spots are found at Io, Europa's aurora is faint suggesting a general difference in how the plasma interaction shapes the aurora at Io and Europa. The dusk side is consistently brighter than the dawnside with only few exceptions, which cannot be readily explained by obvious plasma physical or known atmospheric effects. Brightness ratios of the near-surface O_I 1356 Å to O_I 1304 Å emissions between 1.5 and 2.8 with a mean ratio of 2.0 are measured, confirming that Europa's bound atmosphere is dominated by O₂. The 1356/1304 ratio decreases with increasing altitude in agreement with a more extended atomic O corona, but O₂ prevails at least up to altitudes of ~900 km. Differing 1356/1304 line ratios on the plasma upstream and downstream hemispheres are explained by a differing O mixing ratio in the near-surface O₂ atmosphere of ~5% (upstream) and ≲1% (downstream), respectively. During several eclipse observations, the aurora does not reveal any signs of systematic changes compared to the sunlit images suggesting no or only weak influence of sunlight on the aurora and an optically thin atmosphere.

1. Introduction

Jupiter's moon Europa features various outstanding, distinguishing properties. Within its comparably young and disrupted icy surface [Greeley *et al.*, 2004] it harbors a global liquid water ocean [Khurana *et al.*, 1998; Zimmer *et al.*, 2000; Schilling *et al.*, 2007] and potentially also local shallow water lenses [Schmidt *et al.*, 2011]. Europa's sputtering-generated global atmosphere was theoretically predicted [e.g., Brown *et al.*, 1982; Johnson *et al.*, 1982] and later on observationally confirmed from the far ultraviolet (FUV) emissions at 1304 Å and 1356 Å observed by the Hubble Space Telescope (HST) [Hall *et al.*, 1995]. These oxygen emissions are also studied in this paper. A FUV image taken by Hubble's Space Telescope Imaging Spectrograph (HST/STIS) in December 2012 revealed localized hydrogen and oxygen emissions near the moon's south pole, which indicate the existence of transient eruptions of water vapor [Roth *et al.*, 2014a]. Similar localized emissions could not be identified in subsequent STIS images, suggesting that plume emissions are very rarely detectable by STIS [Roth *et al.*, 2014b] and that such large, yet short-lived plumes are not an important atmospheric source.

The O_I 1356 Å/O_I 1304 Å brightness ratio of 1.3–2.2 of Europa's global oxygen aurora detected by the HST Goddard High Resolution Spectrograph (GHRS) [Hall *et al.*, 1995, 1998] and later on confirmed by STIS [McGrath *et al.*, 2009; Roth *et al.*, 2014a, 2014b] identifies electron impact excitation of atmospheric molecular oxygen (O₂) as the main source of these emissions. For electron impact on O₂ the expected O_I 1356 Å/O_I 1304 Å ratio for an optically thin atmosphere is ~2 over a large range of electron temperatures, whereas electron impact on atomic oxygen (O) and sunlight scattered by the O atoms would imply a ratio well below 1. Based on the

generation from sputtered water ice, the atmosphere mainly consists of some mixture of H₂O, O₂, H₂, OH, O, H, and other H and O compounds [Johnson *et al.*, 2009]. Cassini UV spectra pointed to an extended atomic oxygen cloud above the near-surface O₂ atmosphere [Hansen *et al.*, 2005]. In addition, traces of sodium and potassium were found in Europa's vicinity [Brown and Hill, 1996; Brown, 2001]. A tenuous ionosphere was also measured by the Galileo spacecraft [Kliore *et al.*, 1997] produced from the atmosphere predominantly by electron impact ionization and to a lesser extent by photoionization [Saur *et al.*, 1998].

Europa's FUV aurora is generated by collisions between atmospheric particles and electrons from the time variable magnetospheric environment. Jupiter's magnetic dipole axis is tilted by $\sim 10^\circ$ from its spin axis and so is the magnetic equatorial plane with respect to Jupiter's spin equatorial plane. The planet's fast rotation period causes large centrifugal forces of the corotating magnetospheric plasma, which confine the plasma into a disk—often referred to as the plasma sheet—centered at the centrifugal equator. This centrifugal and plasma sheet equator is tilted from the spin plane by $\sim 2/3$ of the tilt of the magnetic field [Khurana *et al.*, 2004]. With an inclination smaller than 1° , Europa's orbital plane almost coincides with the Jupiter spin plane. Consequently, the magnetic field orientation, plasma flow direction, and plasma density change constantly at Europa over the synodic rotation period of Jupiter of 11.2 h. The velocity of the (almost fully) corotating plasma are substantially higher ($\sim 117 \text{ km s}^{-1}$) than the moon's orbital velocity ($\sim 14 \text{ km s}^{-1}$). The faster orbiting plasma particles interact with the moon's surface and neutral environment in several ways, most important being plasma collisions, which constitute the main atmospheric source and loss processes as we further discuss in this section. Ion neutral collisions also generate a current system in Europa's ionosphere leading to the formation of Alfvén wings [e.g., Neubauer, 1998; Kivelson *et al.*, 2004] above and below Europa. The initially corotating plasma is slowed and diverted around the obstacle. The variable magnetospheric field at Europa also leads to the generation of secondary magnetic fields in the saline, electrically conductive subsurface ocean [Khurana *et al.*, 1998; Zimmer *et al.*, 2000], which additionally perturb Europa's magnetic and plasma environment [Schilling *et al.*, 2007, 2008].

Because of the time variable and perturbed plasma environment, derivation of the atmospheric density and distribution from observations of electron-excited aurora is difficult. Assuming a homogeneous and constant electron density and temperature and an atmosphere confined to the geometric cross section of the visible disk of Europa, Hall *et al.* [1998] infer an O₂ column density of $(2.4\text{--}14) \times 10^{14} \text{ cm}^{-2}$ from the oxygen brightness measured by GHRS. Applying numerical simulations of the magnetosphere-atmosphere interaction and aurora formation and thus accounting for the deflection and cooling of the incoming plasma Saur *et al.* [1998] derive a column density of $5 \times 10^{14} \text{ cm}^{-2}$ from the GHRS brightness of Hall *et al.* [1995]. Thus, the amount of emitted photons is consistent with the thermal magnetospheric plasma being the main excitation source. This means that no local acceleration mechanism is needed to produce the aurora, in contrast to, e.g., the generation of Ganymede's auroral ovals [Eviatar *et al.*, 2001]. A comparison of the Saur *et al.* [1998] simulation results with the first images of the aurora morphology on the trailing hemisphere taken by STIS reveals significant differences of the observed and simulated emission pattern [McGrath *et al.*, 2004, Figure 19.10]. In contrast to the rather symmetric global limb glow in the model results, the observed morphology appears asymmetric and irregular, which can in principle be caused either by an inhomogeneous and patchy atmosphere [e.g., Cassidy *et al.*, 2007] or by an asymmetric electron flow pattern or magnetic field geometry. The oxygen aurora brightness is correlated with Europa's changing position with respect to the plasma sheet [Saur *et al.*, 2011].

Another approach to constrain Europa's atmosphere is provided by modeling efforts of the sources, sinks, and atmospheric chemistry. Erosion (sputtering) and radiation-induced chemical alteration of the surface (radiolysis) are the physical source processes for the atmosphere (see, e.g., reviews by Johnson *et al.* [2004, 2009]). Using laboratory sputtering and kinetic model results, Cassidy *et al.* [2013] find that most of the O₂ (and H₂) production is done by the cold or thermal oxygen ions ($T \sim 100 \text{ eV}$), while the highest H₂O sputtering yield is from higher energy ions (keV to MeV). Not considering changes in surface temperature over a day, Cassidy *et al.* [2013] also find that sputtering of O₂ is confined almost entirely to the trailing (or upstream regarding the plasma flow) hemisphere. Results of a three-dimensional kinetic atmosphere model by Plainaki *et al.* [2013], however, indicate that daily surface temperature variations from the changing solar illumination might in fact play a role for the O₂ sputtering yields besides the incident plasma direction and that the O₂ atmosphere is densest on the dayside and thus time variable. Main loss processes for the bound O₂ atmosphere are atmospheric sputtering by the thermal ions (through charge exchange) and ionization (with the new ions being picked-up by the rotating magnetic field) [Saur *et al.*, 1998]. If the thermal ions lose most of their energy through atmospheric collisions (through charge exchange), a large fraction of

the ions will not reach the surface and the contribution to the surface sputtering might be lower than that estimated by *Cassidy et al.* [2013]. The escape of neutrals from Europa is dominated by thermal escape of lighter hydrogen atoms and molecules [*Shematovich et al.*, 2005; *Smyth and Marconi*, 2006], which therefore presumably form the neutral gas torus detected in Europa's orbit [*Mauk et al.*, 2003; *Lagg et al.*, 2003].

Between November 2014 and April 2015, a Europa STIS observing campaign with FUV aurora observations on 15 days was carried out. Here we analyze the oxygen aurora images taken in this 2014/2015 campaign together with technically identical images previously obtained in 1999, 2012, and in January and February 2014. Various aspects of the oxygen emissions and the simultaneously imaged hydrogen Lyman α emission in the previous visits were studied by *McGrath et al.* [2004], *Cassidy et al.* [2007], *McGrath et al.* [2009], and *Roth et al.* [2014a, 2014b]. There are indications from model results and observations that Europa's near-surface oxygen atmosphere is spatially nonuniform. Interpretation of the morphology of Europa's oxygen aurora with regard to such atmospheric nonuniformities is difficult, as explained earlier. While the general morphology of the same FUV emissions at the neighboring moons Io and Ganymede is already characterized and understood to some level [e.g., *Roesler et al.*, 1999; *Saur et al.*, 2000; *Retherford et al.*, 2003; *Feldman et al.*, 2000; *McGrath et al.*, 2013; *Roth et al.*, 2014b; *Saur et al.*, 2015], Europa's emission pattern is still unclear and poorly understood at present. In this study, we provide the first systematic analysis and characterization of Europa's oxygen aurora brightness, morphology, and time variability. We investigate the influence of the magnetic field and plasma environment, which primarily form the aurora morphology at the neighboring moons Io and Ganymede and search for consistent asymmetries related to the observing geometry. With this work, we also aim to provide the data in a way that allows future atmosphere and plasma interaction simulation studies to compare their results on atmospheric and plasma properties with the UV aurora observations.

The paper is structured as follows: in section 2, we report the new set of 2014/2015 campaign data and explain the data processing and extraction of the analyzed aurora images. Section 3 describes the derived oxygen aurora properties such as brightness, spatial morphology, and temporal variability. In section 4, we discuss the results with respect to the plasma environment and Europa's atmospheric distribution and composition. Section 5 summarizes the most important results.

2. Observations

2.1. Overview

During the 20 HST visits analyzed in this study, STIS obtained spectral images of Europa in the first-order spectroscopy mode with the G140L grating and the $52'' \times 2''$ slit, mapping the moon's entire $\sim 1''$ wide disk at wavelengths between 1190 Å and 1720 Å. An example spectral image over the full wavelength range and spatial dimension, which includes the OI 1304 Å and OII 1356 Å multiplets analyzed here, is displayed in, e.g., Figure 3 of *Roth et al.* [2014b]. During each visit, exposures were taken over several HST orbits and the visit lengths vary between one and five orbits, see Table 1. During the first five visits (until February 2014) two exposures were taken within each orbit, which are analyzed here as one combined orbit exposure or image. On five occasions Europa was observed in eclipse by Jupiter during the entire or parts of the visit, providing the first eclipse STIS spectral images. Europa's eclipse passage takes about ~ 2.5 h, allowing a maximum of two consecutive eclipse HST orbits with the moon in shadow. During two 2-orbit visits Europa was sunlit during one orbit and eclipsed during the other, allowing a direct comparison between the emissions in sunlight and eclipse.

The visits were systematically scheduled at various orbital longitudes of Europa covering different hemisphere views and geometries with respect to the plasma flow, see Figure 1. Whenever the HST scheduling constraints allowed, the visits were timed to cover plasma sheet crossing of Europa, when the moon is also exposed to the largest change of the ambient magnetic field orientation. The plasma sheet crossings coincide with the highest magnetospheric plasma density and therefore presumably with the strongest aurora signal. The five-orbit visits are best suited to track magnetosphere-induced time variability as they cover about 7 h and thus more than half a cycle of Jupiter's synodic rotation period at Europa. Aurora morphology induced by the variable magnetospheric plasma environment should vary over the five orbits of such visit. Europa's orbital longitude (OLG) and thus the subobserver longitude changes by only $\sim 7^\circ$ between the HST orbits and an emission morphology fixed in Europa's planetographic system from, e.g., an atmospheric asymmetry will appear relatively time stationary over the course of a visit.

Table 1. Parameters of the HST/STIS Observation Visits

Visit	Observed Hemisphere	Date ^a	Start Time (UTC)	End Time (UTC)	No. HST Orbits	Total Exp. Time (min)	Used Exp. Time (min)	Europa Diameter (arcsec)	Subobserver W Longitude (deg)	System III Longitude (deg)	FUV Albedo ^b (%)
1	Trailing	1999/10/5	08:39	15:32	5	156.0	156.0	1.07	245–274	300–161	1.5 ± 0.2
2	Trail./Anti-J.	2012/11/8	20:41	03:33	5	183.4	183.4	1.04	209–238	24–244	1.6 ± 0.2
3	Leading	2012/12/30	18:49	01:39	5	164.1	164.1	1.02	79–108	360–220	1.5 ± 0.2
4	Lead./Anti-J.	2014/1/22	14:02	20:53	5	183.4	143.4	1.01	117–146	201–61	1.7 ± 0.2
5	Lead./Anti-J.	2014/2/2	08:19	15:07	5	183.4	123.4	0.99	129–157	199–57	1.7 ± 0.2
6	Trail./Anti-J.	2014/11/7	16:02	19:25	3	131.1	30.7	0.81	224–238	68–176	1.5 ± 0.5
7	Eclipse	2014/11/19	13:10	14:50	2	52.5	31.3	0.84	348–355	208–261	n/a
8	Lead./Sub-J	2014/12/7	20:25	23:56	3	131.1	83.7	0.89	42–57	245–357	1.4 ± 0.3
9	Trail./Anti-J.	2014/12/16	17:46	21:13	3	123.4	78.3	0.91	224–238	244–354	1.4 ± 0.3
10	Ingress/Eclipse	2014/12/17	22:34	00:16	2	72.7	38.7	0.91	345–353	86–141	1.9 ± 0.8
11	Trailing	2015/1/18	00:59	04:36	3	130.9	102.7	0.98	261–276	250–6	1.4 ± 0.2
12	Leading	2015/1/26	22:17	01:55	3	125.5	107.0	0.99	83–98	244–1	1.8 ± 0.2
13	Trailing	2015/2/22	11:00	16:17	4	171.2	154.6	0.98	256–278	132–301	1.4 ± 0.2
14	Leading	2015/2/24	05:58	12:51	5	217.0	195.3	0.98	77–107	67–288	1.9 ± 0.2
15	Trail./Sub-J.	2015/3/9	01:03	08:01	5	232.0	193.4	0.96	296–325	189–52	1.3 ± 0.2
16	Lead./Anti-J.	2015/3/21	16:59	22:21	4	183.3	145.0	0.93	141–163	209–21	1.5 ± 0.3
17	Eclipse/Egress	2015/3/23	23:14	01:12	2	72.6	57.3	0.92	10–18	146–209	1.7 ± 0.6
18	Lead./Anti-J.	2015/3/28	17:42	22:59	4	178.7	124.0	0.91	133–156	216–25	1.6 ± 0.3
19	Eclipse	2015/4/3	15:20	15:51	1	30.6	30.6	0.90	12–14	73–90	n/a
20	Eclipse	2015/4/14	06:08	08:02	2	72.1	54.1	0.87	8–16	318–19	n/a

^aDates are formatted as year/month/day.

^bAlbedos derived between 1430 Å and 1530 Å. No values can be derived for visits in eclipse only.

2.2. Processing

During a portion of each observing orbit, HST is on the Earth's dayside and the obtained data is strongly contaminated by geocoronal airglow, which affects particularly the OI 1304 Å line. On the nightside this contamination is considerably lower. The observations are taken in the TIME-TAG mode and we monitor the OI 1304 Å background signal as HST moves into Earth's shadow and eliminate the most contaminated exposure time in each exposure. Exposure times are equally corrected for both the OI 1304 Å and OI 1356 Å images for comparability, although the OI 1356 Å emissions are hardly affected by geocoronal airglow. The total and reduced exposure times for each visit are shown in Table 1.

A correction to remove the (remaining) geocoronal airglow, other background emissions, and detector noise is performed for all spectral images, explained in detail, e.g., in Roth *et al.* [2014c]. To eliminate the surface-reflected sunlight, model spectral images are generated by mapping the solar UV spectrum from the day of the observation [Woods *et al.*, 1996, 2005] to a homogeneously bright model disk of Europa. The model spectral image is convolved with the STIS point spread function [Krist *et al.*, 2011] and adjusted to match the observed surface reflection signal between 1430 Å and 1530 Å. The derived albedo values (Table 1) are consistent with previous FUV measurements [Hall *et al.*, 1998; Roth *et al.*, 2014a, 2014b]. On the leading hemisphere the weighted mean value (standard deviation) is 1.68% (0.07%) and slightly higher than the weighted mean measured on the trailing hemisphere of 1.47% (0.08%). The small differences might originate from the preferred particle bombardment of the trailing hemisphere, which also causes Europa's strong albedo dichotomy in the visible [e.g., Johnson *et al.*, 2004]. With the found dichotomy, a gradient in reflectivity across the disk is expected in images taken near OLG = 0°/180°. Such hemispheric FUV continuum albedo gradient can not be resolved in the spectral images. The systematic error for the residual emission on one hemisphere from the assumption of a homogeneous albedo is, however, on the order of 1% only.

Finally, quasi-monochromatic $\sim 3 R_E \times 3 R_E$ (Europa radius, $1 R_E = 1560$ km) oxygen emission images centered at the brightest multiplet line each (1302.2 Å and 1355.6 Å) are extracted from the background and

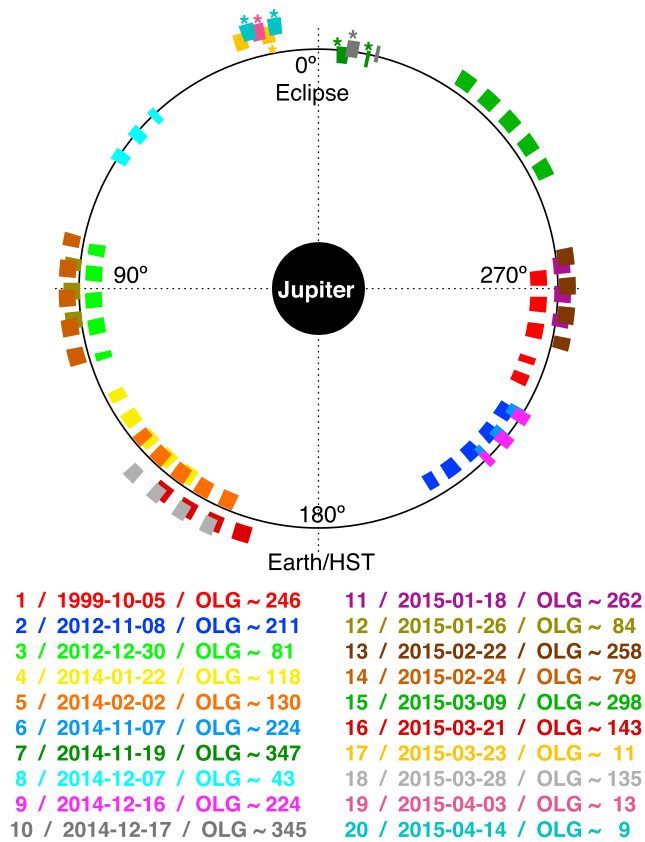


Figure 1. Orbital longitude (OLG) of Europa during the individual exposures of all 20 visits analyzed here. The length of each box representing one exposure (or combined exposures of the same HST orbit) reflects the covered longitudes from start to end of the exposure. Orbits with Europa eclipsed by Jupiter are marked by stars. For more information on the observing parameters see Table 1. The color coding for the 20 visits is used in Figures 5–9. The OLG given below refers to the start of each visit.

reflected-sunlight-corrected spectra and rotated to point Jupiter’s north upward. The secondary lines of the OI 1304 Å triplet are offset by 4 pixels (1304.9 Å) and 6 pixels (1306.0 Å), the secondary line of the OI 1356 Å doublet is offset by 5 pixels (1358.5 Å). The statistical uncertainties of the counts in each pixel are propagated through this processing to account for both the subtracted background emission and reflected sunlight.

In Figures 2 and 3, example OI 1356 Å and OI 1304 Å images taken during two visits of Europa at western and at eastern elongations are shown together with images of the brightness ratio of the two lines. Around western elongation, Europa’s trailing or plasma upstream hemisphere is observed, while near eastern elongation, the leading hemisphere or plasma downstream side/downstream wake is visible to the observer. We analyze both the images taken during the individual HST orbits of one visit and the superposition of all images taken during one visit. The visit superpositions (rightmost columns in Figures 2 and 3) are used to investigate the variation of the oxygen aurora as a function of orbital longitude, as they provide a higher signal-to-noise ratio and the viewing geometry changes by only 30° (five-orbit visit) or less within a visit. Figure 4 shows images when Europa was in eclipse and after egress from eclipse. For the geometric and magnetospheric parameters of the individual and combined images (shown below the displayed images) we use the midpoint of the (superposed) exposure time. Superposed images from the visits from 1999, 2012, and early 2014 can also be found in *McGrath et al.* [2009] and *Roth et al.* [2014a, 2014b]. Images from individual orbits from the previously published visits in 1999 and 2012 are displayed in the Supplementary Material of *Roth et al.* [2014a] and in *McGrath et al.* [2009] (only the 1356 Å images from 1999).

The data is binned and smoothed for display as described in the caption of Figure 2. However, all absolute brightness and brightness ratios stated in the text or shown in plots (Figures 5 to 9) are calculated

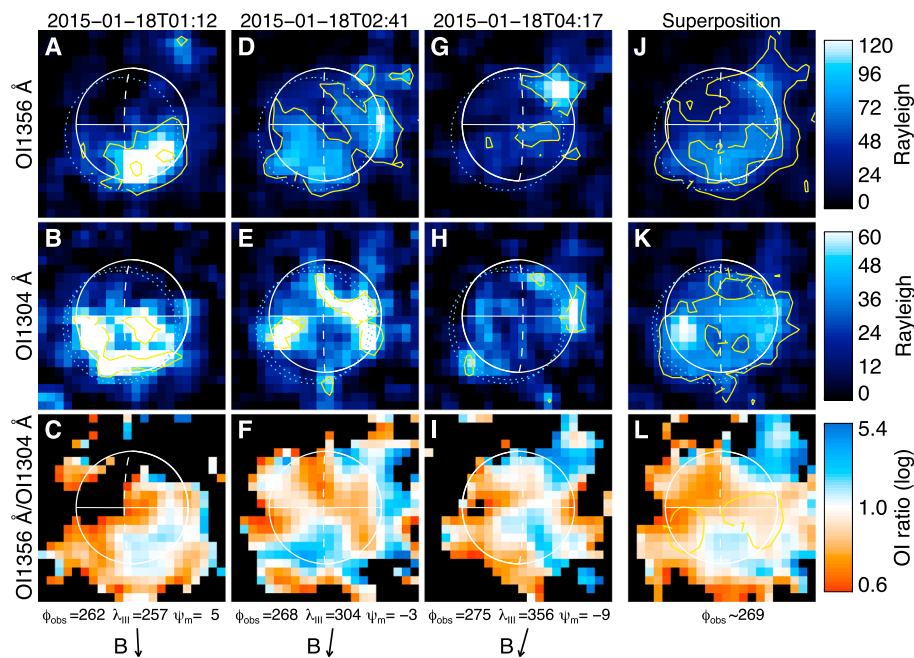


Figure 2. OI 1304 Å, OI 1356 Å and oxygen ratio images from the individual orbits and (right column) the superposition from a three-orbit visit with Europa’s trailing hemisphere at western elongation. The average subobserver W longitude φ_{obs} , System III longitude λ_{III} , magnetic latitude ψ_m (all in degrees), and the projected magnetic field line are given below. The dotted light blue circles indicate Europa’s location for the secondary multiplet lines. The trailing-leading meridian is dashed, the sub-anti-Jovian meridian and equator are solid. The 3×3 pixels are binned and the binned pixels are smoothed as described in the text (for display only!). The yellow contours show signal-to-noise ratios (SNRs) of the binned pixels before smoothing. The ratio images are calculated from heavily smoothed OI 1356 Å or OI 1304 Å images, with pixels with SNR < 0.1 in either oxygen image blackened, and these images hence need to be interpreted with caution. This visit is a good example for magnetosphere-related aurora morphology variability: Europa crosses the plasma sheet center from above to below between the first and third exposures and the aurora brightness moves from the southern hemisphere toward the northern with a rather homogeneous distribution in the plasma sheet center (middle exposure).

without/before any smoothing. The errors of the data points in Figures 5 to 9 are the propagated statistical uncertainties from all pixels in the respectively analyzed area. When we calculate the mean brightness from several images, we use the standard deviation of the sample as error margin (which is then naturally independent of the statistical error of the individual measurement). In some cases, we use the weighted mean instead of the arithmetic mean (stated in the text) and calculate the propagated error after the formula for the weighted mean.

The OI 1356 Å images provide a higher signal-to-noise ratio (SNR) than the OI 1304 Å images for several reasons. First, the atmospheric OI 1356 Å emissions are brighter by a factor of ~ 2 . Second, the lower atmospheric OI 1304 Å brightness is often comparable to the brightness of the (subtracted) surface-reflected light, which is higher at 1304 Å due to higher solar flux. Therefore, the OI 1304 Å images are more strongly affected by potential UV albedo inhomogeneities [McGrath et al., 2009; Roth et al., 2014a]. Third, the geocoronal airglow near 1304 Å is about an order of magnitude higher than near 1356 Å (even in the corrected exposures) and sometimes higher than 100 Rayleighs (R)—compared to ~ 40 R Europa atmospheric emission—due to the scattered light from geocoronal atomic oxygen. Additionally, the opacity of the atmospheric atomic oxygen column to 1304 Å could be nonnegligible and scattered sunlight from oxygen atoms on the order of a few Rayleighs is expected at 1304 Å possibly skewing the plasma-induced aurora morphology signal to be analyzed. Therefore, we will use primarily the OI 1356 Å images for the detailed morphology analysis but also investigate the OI 1304 Å emission with respect to the observed brightness of the combined exposures of the visits and the brightness ratio OI 1356 Å/OI 1304 Å. We find that the OI 1304 Å morphology—while noisier—generally resembles the OI 1356 Å morphology.

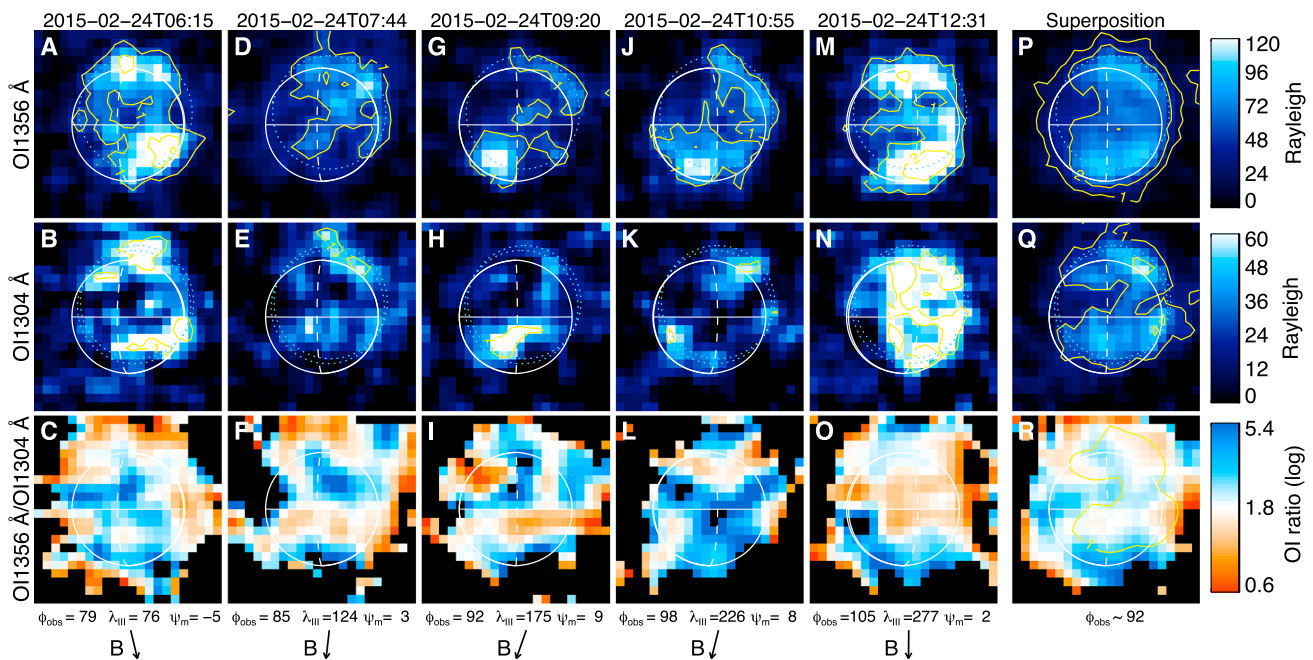


Figure 3. Individual orbit images and visit superposition images from a five-orbit visit of Europa’s leading hemisphere at eastern elongation. The emission morphology is relatively symmetric with respect to the changing magnetic field orientation during this visit. Brightest emissions are near the magnetic poles (see text), while the emissions at the left and right flank near the equator (where Io’s bright aurora spots are located) are faint. For more information see Figure 2.

3. Results

3.1. Total Aurora Brightness

3.1.1. Global Brightness

An overview of the total brightness from all 71 orbit images can be found in Figure 5. There we show the derived total OI 1304 Å and OI 1356 Å brightness with propagated statistical uncertainties as a function of the Jovian System III longitude (Figures 5a and 5b) and Europa’s distance to the plasma sheet center (Figures 5c and 5d). By total brightness we refer to the total photon flux measured within $1.25 R_E$ around Europa’s center at the brightest multiplet line (1302.2 Å and 1355.6 Å, respectively) and normalized to the cross section of Europa’s disk (πR_E^2). Similar or equivalent definitions for such disk averages were previously used to quantify the total flux or total brightness [e.g., Hall et al., 1998; Roth et al., 2014a].

The brightness undergoes considerable variations between the visits and also between the orbits within each visit. The maximum and minimum total brightness are 158 R and 33 R for OI 1356 Å, and 96 R and 12 R for OI 1304 Å. Figures 5a and 5b show a systematic variation with Jupiter’s rotation period: The brightest emissions are detected near the plasma sheet crossings of Europa, which occur around 106° and 286° after the VIPAL magnetic field model by Hess et al. [2011] or at 111° and 291° after the VIP4 model by Connerney et al. [1998]. From here on, we will use the VIPAL model as reference model for the magnetic field. However, for our analysis the difference between both models is very small and will not change any conclusions of this paper. Example images for brightening during plasma sheet crossings can be found in Figure 3, where the OI 1356 Å aurora considerably brightens between the second last (K) and last (N) orbit of the visit.

Both the OI 1356 Å and OI 1304 Å brightness in the bins around the plasma sheet crossing at $\sim 110^\circ$ are slightly higher than around the other crossing near $\sim 290^\circ$ (Figures 5a and 5b). The standard deviations from the mean brightness in the two bins near the plasma sheet crossings are, however, larger than the difference, preventing a firm conclusion.

From the System III longitude λ_{III} , we calculate the magnetic latitude for each data point through $\psi_m = \psi_0 \cos(\lambda_{III} - \lambda_{III}^0)$ with the System III longitude of Jupiter’s magnetic south pole $\lambda_{III}^0 = 196^\circ$, and the tilt between the magnetic and polar axes $\psi_0 = 9.8^\circ$ for the VIPAL model. An absolute distance of Europa from the centrifugal equator is then calculated by $z_c = d_{Jup} \tan(2/3 \psi_m)$ [Hill et al., 1974], where d_{Jup} is the distance to Jupiter’s barycenter. Figures 5c and 5d show that the aurora brightness on average steadily decreases for larger z_c , although the scattering around the means (black histogram) in each longitude bin is high.

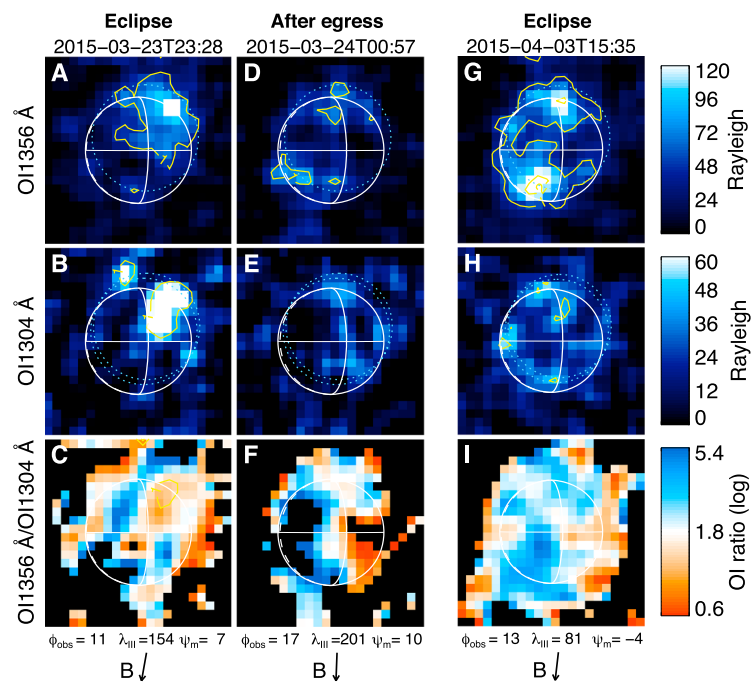


Figure 4. Individual exposures from (a–f) eclipse/egress visit 17 and (g–i) eclipse visit 19. The aurora is fainter during visit 17 than during visit 19 as expected from the larger distance of Europa and the lower ambient plasma density during the former visit. No general differences of the morphology or brightness are found compared to observations in sunlight, and the brightness during visit 17 decreases after egress (compare Figures 4a and 4b to 4d and 4e) as Europa’s distance to the plasma sheet increases. Because of the particular observing geometry in eclipse, the usually observed north-south brightness asymmetry appears inverted in the images (see text), which explains the brighter emission in the north in Figures 4a and 4b, although Europa is above the plasma sheet.

To compare aperiodic brightness changes within a visit (time scale of minutes/hours) to the changes between visits (time scale of days, weeks, or months), we first normalize the brightness of each individual orbit exposure by subtracting the respective fitted value (dashed line in Figure 5) in order to eliminate the periodic variations. The standard deviation of the normalized brightness of all exposures in a single visit is a measure of the aperiodic variability within that visit. The mean of these standard deviations for all visits then gives the average deviation from the fitted profile. This should be compared to a measure of the variability among the visits. For this, we averaged the normalized brightness within each visit and calculated the standard deviation of these means over all visits.

Taking into account the OI_I 1356 Å images of only visits with 3, 4, or 5 orbits, we find that the mean of the standard deviations is 17.2 R and the standard deviation of the mean values is 17.3 R. Changes within the visits that last a few hours are thus similar to changes from one visit to the next, i.e., on time scales of days, weeks, or months. For comparison, the mean statistical uncertainty of the derived brightness per orbit is 4.1 R and considerably lower.

One noticeable overall deviation is the aurora brightness during the October 1999 visit, where all measured values are higher than almost all other measurements at similar System III longitudes. The 1999 brightness exceed the mean values of the respective bins by more than the standard deviation.

Figure 6 shows the brightness measured in the superpositions of all exposures from each visit. The brightness of the 1999 visit also significantly exceeds the mean values in the same longitude bin by 60% for OI 1304 Å and 50% for OI_I 1356 Å. The 1999 values are therefore excluded from the calculated mean, as we currently aim to analyze the effects of the orbital positions and not long-term changes, which are apparently present between 1999 and the 2012–2015 period. However, including the one 1999 value would change the results insignificantly. Relatively high total brightness were also measured in the 2012 observations, but no significant, consistent brightness changes from November 2012 to April 2015 are found.

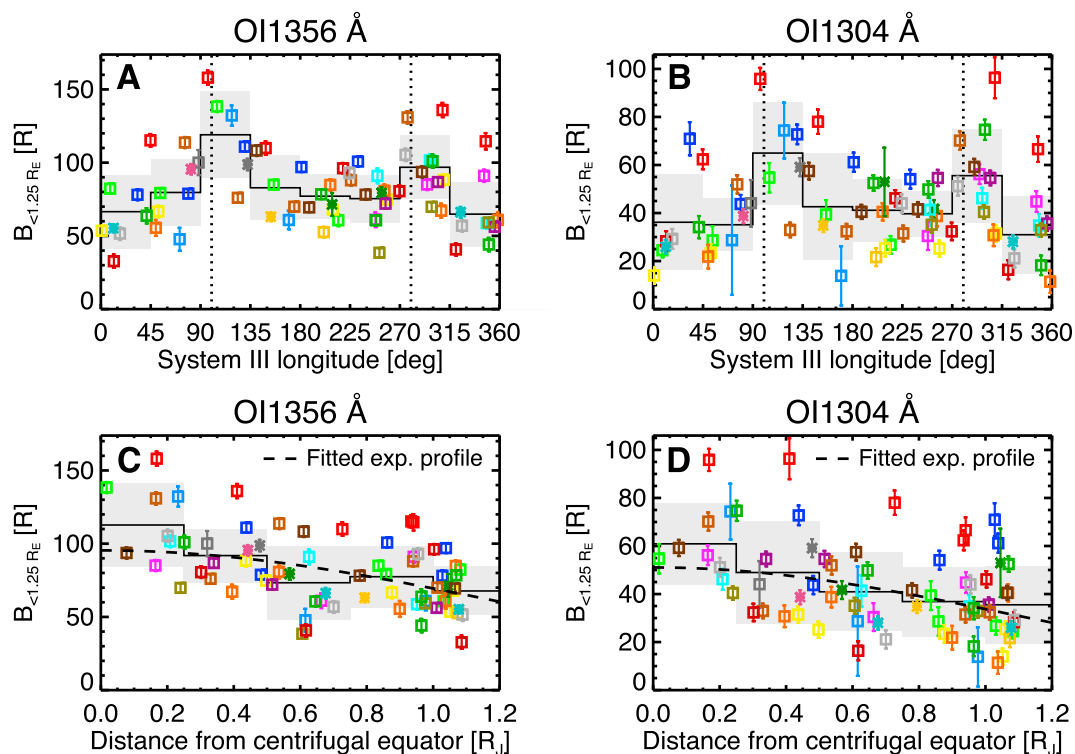


Figure 5. Total OI] 1356 Å and OI 1304 Å brightness measured within 1.25 R_E and normalized to the cross section of the disk as a function of (a and b) Jupiter's System III longitude and (c and d) Europa's distance to the centrifugal equator in Jupiter radii (R_J). The solid lines show the arithmetic mean of the measurements in 45° wide (Figures 5a and 5b) and 0.25 R_J wide (Figures 5c and 5d) bins, the standard deviation from the mean within each bin is shown in shaded grey. Vertical dotted lines (Figures 5a and 5b) show Europa's plasma sheet crossing. The dashed curves (Figures 5c and 5d) are the fitted brightness profiles given in equation (2). For the color coding of the visits see Figure 1.

The OI] 1356 Å brightness is similar on the trailing/upstream and leading/downstream hemisphere visits. The OI 1304 Å aurora is on average fainter during the leading/downstream hemisphere visits than on the trailing/upstream hemisphere (even with the bright 1999 trailing hemisphere observation excluded). This is not directly obvious from Figure 6b, where the uncertainties (shaded areas) of longitude bin averages around 90° (leading) and 270° (trailing) slightly overlap. However, the mean 1304 brightness of all western elongation

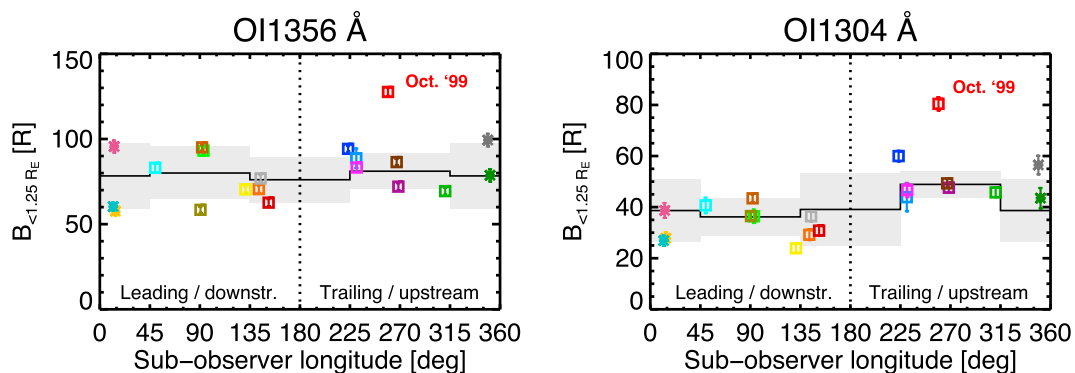


Figure 6. Total oxygen brightness as function of the subobserver W longitude. Visits partly or fully in eclipse are displayed with stars. The histogram shows the mean within the longitude bins with the standard deviation from the mean in shaded grey. The October 1999 visit (red) is not taken into account for the mean, as the brightness appears to be systemically higher, see text. While no considerable brightness differences between leading and trailing hemispheres are found at (a) OI] 1356 Å, the (b) OI 1304 Å brightness is lower on the leading side. For the color coding of the visits see Figure 1.

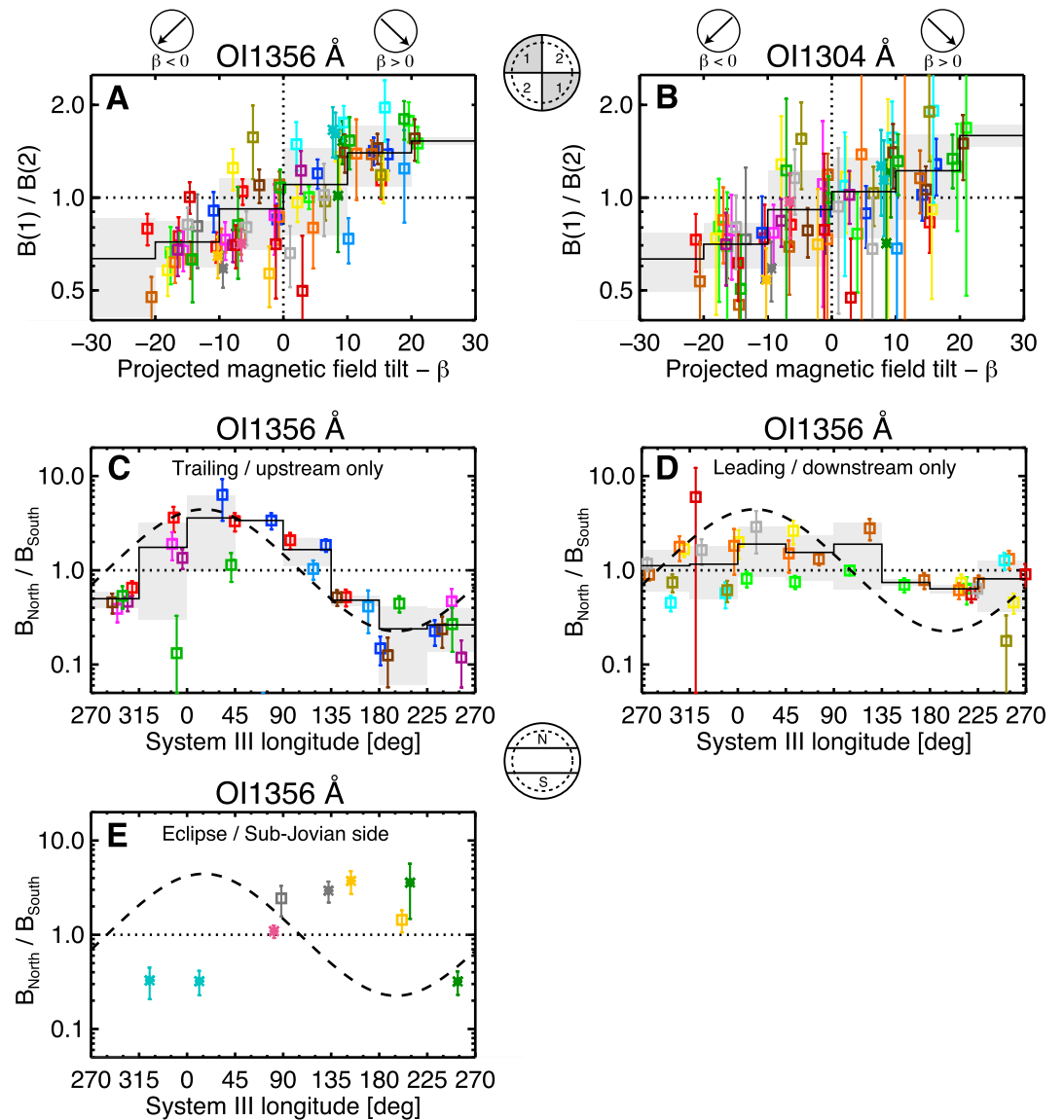


Figure 7. (a, b) Ratio of the combined brightness of the two oppositely located quadrants “1” to quadrants “2” as function of the angle β between the projected magnetic field and the north-south line. Brightness ratio of the north polar region to the south polar region at latitudes $>30^\circ$ N/S as function of System III longitude for the OI] 1356 Å aurora images around (c) western ($20^\circ < \varphi_{\text{obs}} < 160^\circ$) and (d) eastern ($200^\circ < \varphi_{\text{obs}} < 340^\circ$) elongation, and (e) near/in eclipse. The compared regions are sketched in the middle with the dashed line that shows Europa’s disk and solid is at $1.25 R_E$. The dashed curve (Figures 7c–7e) shows the relative content of the electron energy reservoirs above and below Europa as proxy for the expected brightness ratio, see text. Means (black histogram) and standard deviations (shaded grey) are shown for 10° wide (Figures 7a and 7b) and 45° wide (Figures 7c and 7d) bins. Europa’s oxygen aurora is brightest near the magnetic poles, i.e., where the magnetic field line bisecting Europa intersects the polar region (Figures 7a and 7b). On the trailing side the hemisphere facing the plasma sheet is on average brighter than the opposite hemisphere (Figure 7c). For the color coding of the visits see Figure 1.

visits ($\text{OLG} > 180^\circ$) of $51 \pm 6 R$ is significantly higher than the mean of the eastern elongation visits ($\text{OLG} < 180^\circ$) of $34 \pm 6 R$.

3.1.2. Brightness in Eclipse

The brightness measured in the individual eclipse exposures (stars in Figures 5a and 5b) is similar to the other brightness detected at similar System III longitudes and no systematic deviation is indicated. The larger spread of the *superposed* image brightness near eclipse (i.e., in the bin around $\varphi_{\text{obs}} = 0$ in Figure 6) results from the shorter visits in or near eclipse: While for visits of three or more HST orbits brightness changes due to the local

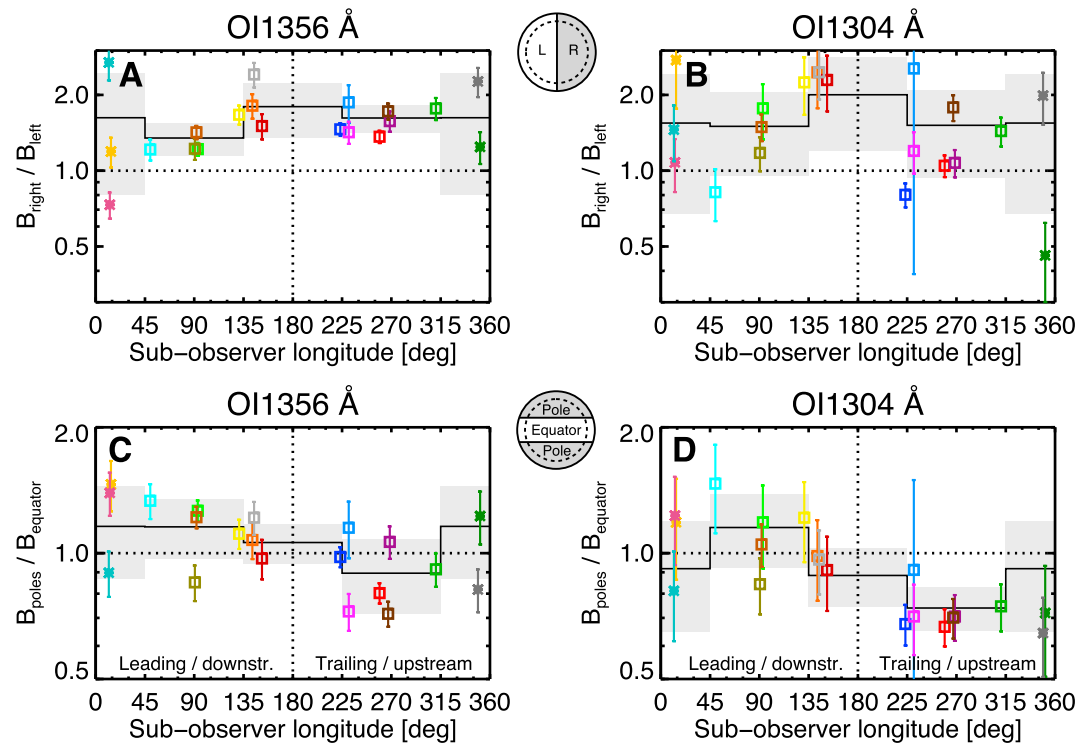


Figure 8. Brightness ratios of (a, b) the right-hand side hemisphere by the left-hand side hemisphere in the images and of (c, d) the polar regions (latitude > 30°) by the equatorial region (latitude ≤ 30°) as a function of the subobserver/orbital longitude. Visits partly or fully in eclipse are displayed with stars. The compared regions are sketched in the middle with the dashed line that shows Europa’s disk, and solid is at 1.25 R_E. The mean brightness in four bins around 0° (near/in eclipse, sub-Jovian hemisphere), 90° (leading), 180° (near transit, anti-Jovian), and 270° (trailing) shows that the aurora is more concentrated toward the equator on the plasma upstream trailing hemisphere than in the plasma wake or leading hemisphere. The right-hand side is consistently brighter for all observing geometries with very few exceptions. The standard deviations from the means are shown shaded grey. For the color coding of the visits see Figure 1.

plasma density variations discussed above are averaged out to some extent, the average brightness of the short eclipse visits depends more strongly on plasma environment at the time of the exposures.

During visit 10, Europa was observed before ingress into eclipse during one orbit and in eclipse during the second at similar distances to the plasma sheet center. The OI 1356 Å brightness did not change between the two orbits and the OI 1304 Å brightness is higher in eclipse but is consistent with constant brightness within

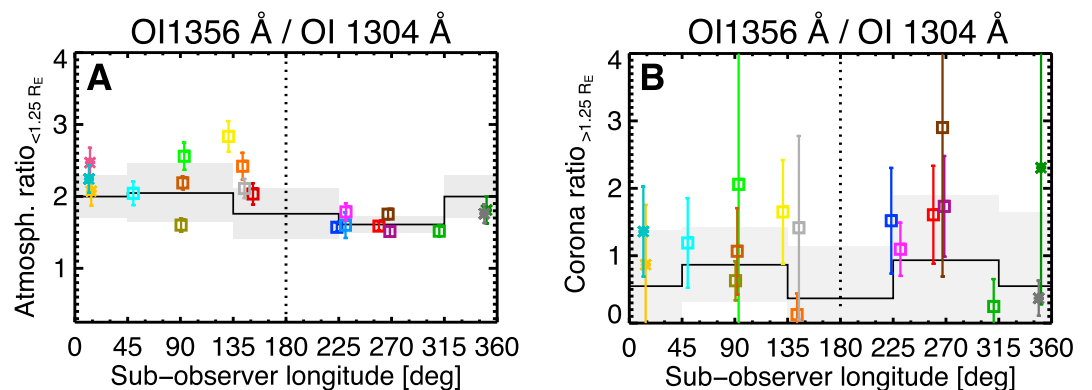


Figure 9. Ratios of the total OI 1356 Å to OI 1304 Å brightness for (a) near-surface atmosphere (all pixels < 1.25 R_E from disk center) and for (b) the corona (pixels between 1.25 and 1.5 R_E), as function of the subobserver W longitude on Europa. For the color coding of the visits see Figure 1.

the uncertainties, see dark grey square (before egress, $\lambda_{III} \sim 90^\circ$) and star (eclipse, $\lambda_{III} \sim 135^\circ$) in Figures 5a and 5b. During visit 17, Europa exited eclipse between the first and second orbits being located above the plasma sheet center. Both oxygen brightness are slightly lower after egress (Figure 5, light orange) in agreement with the larger distance of Europa to the plasma sheet in the second orbit (see parameters below images in Figures 4a–4f). The brightness during the eclipse image taken when Europa was closer to the plasma sheet (visit 19, Figures 4g and 4h) is brighter than during visit 17 following the above derived trend. None of the measured eclipse brightness deviates from the average brightness in the System III longitude bins by more than the standard deviation of all data points; i.e., all eclipse data points (stars) lie within the shaded areas in Figures 5a and 5b. Taken together, there is no indication that the oxygen aurora brightness in eclipse is different from the aurora in sunlight.

3.2. Morphology

3.2.1. Variations With Jupiter's Rotation Period

We again analyze the images of the individual orbits first to discuss morphology changes on the time scale of the magnetosphere variations and then to derive correlations with Europa's changing location with respect to the plasma sheet and the varying magnetic field orientation. By projecting the ambient field direction onto the disk of Europa we create a magnetic coordinate system. We define the "magnetic poles" where the Jupiter's magnetic field is normal to the disk, and the "magnetic equator" where the unperturbed magnetic field is tangential to the disk of Europa.

In most images the brighter emissions are found near the magnetic poles at higher latitudes, while the emissions at Europa's flanks near the magnetic equator are clearly fainter, see, for example, Figure 3. Figures 7a and 7b show the relative brightness of opposed quadrants as a function of the tilt of the projected magnetic field from pointing straight downward. (Note that all ratios are calculated with surface normalized brightness; i.e., the pixel brightness is normalized to the covered area.) A systematic behavior is apparent in that the two quadrants containing the magnetic poles are brighter than the opposite quadrants. The figures also illustrate that the projected tilt of the ambient field from the north-south direction is positively correlated to the brightness in the quadrant containing the magnetic poles. In other words, the two quadrants that contain the magnetic equator are fainter than the quadrants containing the (orthogonal) magnetic field line bisecting Europa. The emissions are gathered around the bisecting field line and not around the magnetic equator like that at Io.

We also find that the aurora is brighter on the hemisphere that faces the plasma sheet center than on the opposite hemisphere in most images. For example, when Europa is above the plasma sheet (positive magnetic latitude ψ_m), the aurora in the southern hemisphere is brighter (Figure 2a), and vice versa (Figure 2c). In about 25% of the images (both lines) the north/south ratio does not strictly follow this trend (e.g., Figure 3d), where aurora on the plasma sheet facing hemisphere is fainter. The north/south hemisphere ratio of both oxygen lines is, however, on average >1 when Europa is farthest below the plasma sheet ($\lambda_{III}=16^\circ$), and <1 when the moon is farthest above the plasma sheet ($\lambda_{III}=196^\circ$). These systematic north/south brightness changes are more pronounced on the trailing hemisphere and in all but one of OII 1356 Å trailing hemisphere images the brightness ratio is close to the expected ratio from Europa's position above or below the plasma sheet (Figure 7c). On the leading hemisphere the north/south ratio is less variable, and systematic correlation with System III longitude is only very weak and hardly detected (Figure 7d).

3.2.2. Eclipse Morphology

In the eclipse images, the ratios deviate strongly from the expected north/south trend (Figure 7e), which might be explained by the observing geometry. A simplified sketch of the brightness ratio is shown in Figure 10 together with two example images at western elongation. As explained, the brightest emissions often coincide with magnetic pole region, with the hemisphere facing the centrifugal equator being brighter. The illustrated geometry shows Europa at western elongation for an observer looking onto the displayed plane. For eclipse observations the observer would be to the left in the sketch. For this geometry the brighter, plasma-sheet-facing hemisphere is shifted behind Europa, while the fainter hemisphere is shifted toward the observer. Therefore, the measured brightness ratio might appear to be inverted with most emissions measured on the hemisphere that is more visible to the observer but not the hemisphere where more emissions are excited in total. Note that the observed brightness ratio also differs more strongly from the proposed theoretical ratio for sunlit visits farther away from maximum elongation of Europa, like visit 7 (Europa at OLG $\sim 315^\circ$, green points in Figure 7e). In other words, the agreement of the observed and proposed theoretical north-south ratios depends on the orbital longitude with less good agreement near OLG = 0° . This general

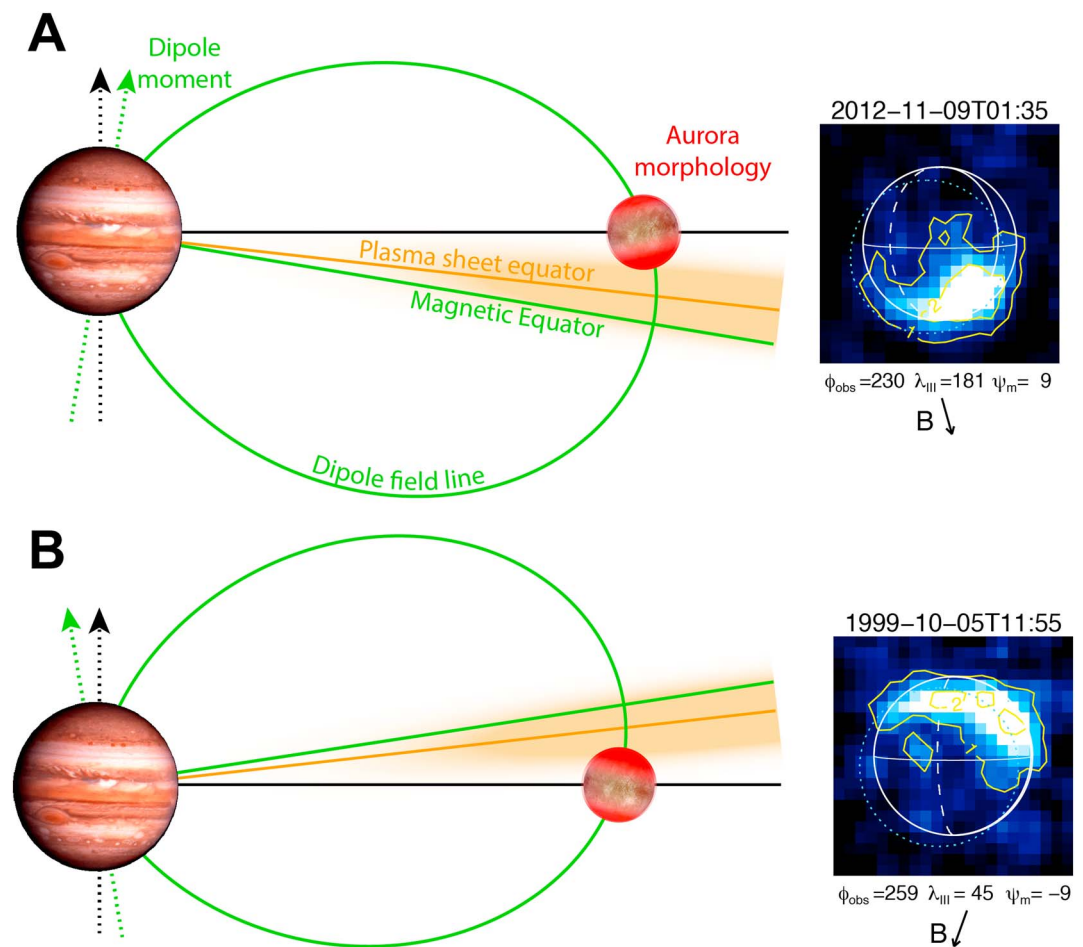


Figure 10. Illustration of the brightest aurora areas for Europa above (A) and below (B) the plasma sheet center and two example OI 1356 Å images with Europa at high and low magnetic latitude ψ_m . The plasma sheet electron density sketched by the diffuse orange area peaks at plasma sheet equator and decreases vertically. In many STIS images the aurora morphology appears to resemble a broadened limb glow that is brighter on the hemisphere that faces the plasma sheet. Emissions around Europa’s equator near the tangential points of the magnetic field to the disk are fainter than the emissions near the magnetic poles. The north-south asymmetry is caused by an inequality of the energy electron reservoirs above the hemispheres, as explained in detail for Io by [Retherford et al., 2003]. For more information on the observation images, see Figure 2.

OLG dependency in all images supports the hypothesis that projection/occultation effects play a crucial role for the observed ratio away from maximum eastern and western elongation.

Besides the inverted north-south asymmetry, general morphology differences between eclipse and sunlit images are not detected.

3.2.3. Changes With Orbital Longitude

We now compare the superposed visit images at different orbital longitudes of Europa corresponding to different geometries of the observed hemisphere. Figures 8a and 8b show a general trend for the morphology in the combined visit images: With only few exceptions the aurora is consistently brighter on the right-hand side hemisphere than on the left-hand side hemisphere. For the OI 1356 Å emission, there is only one eclipse visit, where the left hemisphere is brighter. This measurement can be considered an outlier, as the morphology in the superposed exposures of the eclipse visits are more strongly affected by variable magnetosphere-related effects and thus less suited to investigate general orbital position effects (as explained in section 3.1). The ratios of the right hemisphere brightness by the left hemisphere brightness are similar for both oxygen lines with mean values (standard deviations) of 1.59 (0.33) for OI 1356 Å and 1.66 (0.63) for OI 1304 Å for all visits out of eclipse. Note that the left and right hemispheres as defined for this analysis and Figures 8a and 8b are fixed in the image frames and independent of the observing geometry. The right-hand side thus

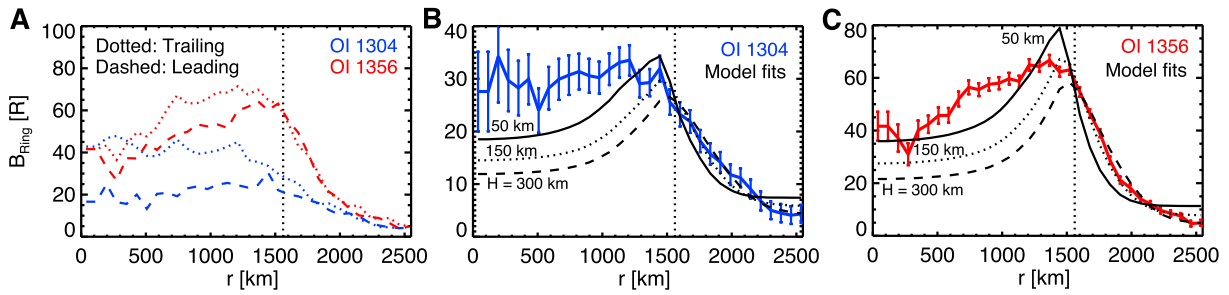


Figure 11. Radial brightness profiles of the mean OI] 1356 Å (red) and OI] 1304 Å (blue) brightness in concentric 0.05 R_E wide rings from disk center (0 km) to 1000 km above the limb (2560 km) as measured on average in all exposures. (a) While the profile above the limb (dotted vertical line) is nearly identical for the visits of the trailing (colored dotted) and the leading hemispheres (colored dashed) as expected, the on-disk emission is brighter on the trailing or plasma upstream hemisphere than on the leading or downstream hemisphere. (b and c) Modeled brightness profiles for radially symmetric exponential aurora profiles with scale heights of 50 km (solid black), 150 km (dotted), and 300 km (dashed) fail to reproduce both the on-disk and above-limb profiles simultaneously. Error bars in Figure 11a are similar to Figure 11b and Figure 11c, respectively, for OI] 1304 Å and OI] 1356 Å, and not shown for better visibility. (Note that the model profile maxima are shifted from the limb onto the disk by the PSF conversion.)

corresponds to the anti-Jovian (sub-Jovian) hemisphere when Europa is at western (eastern) elongation and to the upstream (downstream) hemisphere near eclipse (transit). In terms of local time on Europa, the brighter right hemisphere always coincides with the afternoon or dusk region, while the left hemisphere corresponds always with the morning/dawn region.

We also derive a systematic difference between leading and trailing hemispheres: Toward the center of the disk on the trailing or plasma upstream hemisphere the oxygen emissions are often similarly bright or brighter than the polar emissions (e.g., Figures 2j and 2k). Note that we always refer to surface brightness and do not account for projection effects, e.g., for differing line-of-sight atmospheric column densities between lower and higher latitudes. In the wake of Europa, i.e., in the center on the leading hemisphere, the emissions near the equator are relatively faint compared to the polar regions (e.g., Figures 3p and 3q). The average brightness ratio of the polar region (mean pixel brightness at latitudes $>30^\circ$) by the equatorial region (mean pixel brightness at latitudes $\leq 30^\circ$) in the superposed visit images confirms this trend (Figures 8c and 8d): For both oxygen emissions the equatorial aurora is overall brighter on the plasma upstream/trailing side, while the polar aurora dominates the downstream/leading side morphology. The difference is more pronounced for the OI] 1304 Å line where the pole/equator ratio is higher by a factor of 1.6 on the leading side (Figure 8c), compared to 1.3 for OI] 1356 Å (Figure 8d), suggesting a particularly low OI] 1304 Å emission in the wake.

3.2.4. Radial Brightness Profile

Figure 11 also illustrates this brightness difference between leading and trailing hemispheres. The displayed radial profiles are generated by averaging over all pixels within concentric rings of equal width in the visit images. We then calculate the mean ring brightness for the visit images with propagated uncertainties. Figure 11a shows the profiles for the visits at eastern ($20^\circ < \text{OLG} < 180^\circ$) western elongation ($180^\circ < \text{OLG} < 340^\circ$) separately, Figures 11b and 11c show the profiles for all visit images (both at eastern and western elongation excluding the eclipse images).

While above and near the limb the measured brightness on leading and trailing side are similar, the OI] 1356 Å brightness is slightly lower on the leading hemisphere and the OI] 1304 Å profiles differ more significantly. Near the disk center on the trailing or upstream hemisphere the OI] 1304 Å brightness becomes even similar to the OI] 1356 Å brightness implying a 1356/1304 ratio as low as 1. Figures 11b and 11c show both profiles for all visits combined in comparison to model profiles and are discussed in section 4.2. We will discuss the brightness profiles further and compare them to simple model profiles in section 4.

3.3. Oxygen Line Ratio

The bottom rows of Figures 2–4 show the ratio of the OI] 1356 Å brightness to the OI] 1304 Å brightness color coded such that high ratios (relatively brighter OI] 1356 Å) are blue and low ratios (brighter OI] 1304 Å) are red. For the displayed ratio images, the OI] 1356 Å and OI] 1304 Å images were smoothed applying 6 times a filter of the form

$$f(i_x, i_y) = \frac{1}{8}(4f(i_x, i_y) + f(i_{x-1}, i_y) + f(i_{x+1}, i_y) + f(i_x, i_{y-1}) + f(i_x, i_{y+1})), \quad (1)$$

Table 2. Weighted Mean Oxygen Brightness and Corresponding Uncertainty of the Weighted Means Calculated With the Statistical Error of Each Visit Image (in Parentheses)^a

Region	Distance Range From Disk Center	1356/1304 Ratio			O Mixing Ratio ^c
		All Visits ^b	West. Elong. ^b	East. Elong. ^b	
Near-surface ^d	$r < 1.25 R_E$	1.77 (0.04)	1.63 (0.05)	2.10 (0.07)	<1–6%
High altitude	$1.25 R_E < r < 1.5 R_E$	1.22 (0.11)	1.28 (0.16)	1.18 (0.14)	13–15%
Corona	$1.5 R_E < r < \sim 1.6 R_E$	0.75 (0.13)	0.83 (0.19)	0.68 (0.17)	27–35%

^aLast column: Atomic oxygen mixing ratio range for the 1356/1304 ratios.

^bVisits where any of the derived total brightness is below zero (e.g., due to an overestimation of the subtracted background) are excluded. Values are the means of the individual ratios calculated for each visit and can considerably differ from the ratio of the mean brightness like, for example, displayed in Figure 11.

^cO mixing ratio range in an optically thin O + O₂ atmosphere and corona to reproduce the 1356/1304 ratios by electron impact (dissociative) excitation of O and O₂ assuming two exciting electron populations at 20 eV (95%) and 250 eV (5%). The given range reflects the difference between the values measured at western and eastern elongations.

^dThe near-surface area corresponds to the region measured within $<1.25 R_E$ of the disk center in the 2-D images and thus includes high-altitude coronal emissions in front of the disk as seen from the observer.

where $i_{x/y}$ denote the pixel on the detector x and y axis. Pixels with SNR below 0.1 in either the OII 1356 Å or OI 1304 Å image are blackened. This smoothing is needed to suppress the large statistical fluctuations across the images, which would otherwise make the images noisy and unreadable. Therefore, these images need to be interpreted with great caution. We note again that the images are smoothed only for display, and all derived and discussed values are calculated before any smoothing or binning.

We find two general trends in the line ratio images: First, regions of high ratios are often located near or on the disk, where bright aurora is detected in both lines. For example, the polar regions in the superposed visit image of Figure 3 are bright in both oxygen lines and the line ratio around the poles is also high compared to the image average. And second, the ratio is overall lower in the corona, which is obvious as farther away from the disk red pixels prevail in most images. We now analyze the brightness ratio more quantitatively in larger areas of the individual orbit and superposed visit images.

Ratios of the total OII 1356 Å brightness to OI 1304 Å brightness between 1.5 and 2.8 are measured in the superposed visit images (see Figure 9) with an arithmetic mean (standard deviation) of 2.0 (0.4) for all 20 visits. Since a hemispherical OI 1304 Å brightness difference between leading and trailing hemispheres was found for OI 1304 Å but not for OII 1356 Å different brightness ratios are consequently measured on the two hemispheres (Figure 9a). Higher ratios, i.e., relatively lower OI 1304 Å emissions, were almost consistently measured at eastern elongation ($\varphi_{\text{obs}} < 180^\circ$) with a mean (standard deviation) of 2.3 (0.3) for all visits at longitudes of $\varphi_{\text{obs}} < 180^\circ$. All measured ratios are above 2 except for one visit (visit 12). At western elongation ($\varphi_{\text{obs}} > 180^\circ$), in contrast, the mean of 1.6 (0.1) is significantly lower and all ratios are between 1.5 and 1.8. The mean ratio (standard deviation) of the individual exposures taken completely in eclipse is 2.0 (0.4) and agrees exactly with the values derived for all visits throughout Europa's orbit.

Generally, the oxygen ratio decreases with increasing distance from the surface. Figure 9b shows the brightness ratio at higher altitudes in a region between $1.25 R_E$ and $1.5 R_E$ from the disk center. To compare near-surface and coronal regions, we calculate the weighted mean brightness from all visits in three regions: (1) the total oxygen brightness at $r < 1.25 R_E$, (2) in a high-altitude region at $1.25 R_E < r < 1.5 R_E$, and (3) in a coronal region at $1.5 R_E < r < \sim 1.6 R_E$. The calculated brightness is summarized in Table 2. The measured brightness at higher altitudes in the corona are low and several measured ratios therefore have very low SNR. Hence, the weighted mean provides a more reliable estimation than the arithmetic mean for this comparison.

Note that the weighted means outside the disk are similar and consistent within the uncertainties for the eastern and western elongation observations. The near-surface ratios, in contrast, differ significantly between eastern and western elongation for the weighted means as discussed earlier in this section.

4. Discussion

In this section, we relate our findings to effects of and implications for both Europa's plasma environment and oxygen atmosphere and compare them to previous measurements. We first analyze and describe the

magnetospheric environment, which appears to predominantly control both brightness and morphology of the aurora.

4.1. Magnetospheric Environment

4.1.1. Systematic Variation of Aurora and Plasma Environment

The coincidence of bright aurora with plasma sheet crossings (Figure 5), i.e., Europa is at low magnetic latitudes, confirms the previously observed [Saur *et al.*, 2011] trend that the aurora brightness decreases with increasing distance of Europa to the plasma sheet center. A very similar brightness profile was found for Io's [OI] 6300 Å aurora with two maxima near the plasma sheet crossings and slightly higher emissions around 110° [Oliver *et al.*, 2001]. The density in the plasma sheet peaks near the centrifugal equator and decreases toward higher magnetic latitudes [e.g., Khurana *et al.*, 2004]. The electron temperature profile was shown to be inverted to the density profile with increasing temperatures further from the centrifugal equator [Meyer-Vernet *et al.*, 1995] and does therefore not cause lower brightness at higher latitudes. Thus, the ambient density is likely the parameter that predominantly controls the aurora brightness.

To quantify the brightness dependence on Europa's magnetic latitude and relate it to the vertical plasma sheet density profile, we analyze the brightness as a function of the absolute distance of Europa to the plasma sheet equator z_c . We assume that the aurora brightness is proportional to the ambient plasma density, which can be modeled by a symmetric Gaussian profile with a latitudinal scale height H_c [Hill and Michel, 1976]. We then fit a theoretical brightness profile function given by

$$B(z_c) = B_0 e^{-(z_c/H_c)^2} \quad , \quad (2)$$

to the total brightness measured during each HST orbit, where H_c and B_0 are the fitting parameters. For the OII 1356 Å line, the fit yields a maximum brightness in the plasma sheet center of $B_0 = 96 \pm 2$ R and a characteristic length of $H_c = 1.8 \pm 0.1 R_J$ (Jupiter radius) for the decrease in brightness with increasing plasma sheet distance, see dashed lines in Figures 5c and 5d. The fitted sheet center OI 1304 Å brightness is lower with $B_0 = 51 \pm 3$ R and the OI 1304 Å scale height similar with $H_c = 1.6 \pm 0.1 R_J$.

With the assumption that the aurora brightness profile is proportional to the vertical plasma density profile, the fitted characteristic length can be compared to a vertical scale height of the plasma sheet. In their phenomenological plasma torus model, Bagenal and Delamere [2011] find a vertical scale height of $H_c = 1.7 R_J$ near Europa's orbit, which our values are well in agreement with.

However, we also found a significant variability from exposure to exposure within the visits, after we have subtracted the expected brightness profile after equation (2). This is not surprising, as the density distribution around the plasma sheet will not be as symmetric as the assumed Gaussian profile in equation (2). Significant density asymmetries were measured in the Io torus [e.g., Schneider and Bagenal, 2007; Smyth *et al.*, 2011] and likely are similarly present near Europa. A corotating azimuthally inhomogeneous plasma sheet density could at least partly explain the detected variability in the normalized brightness from exposure to exposure within the visits.

Additionally, aperiodic variations between the visits (of similar magnitude than within the visits) are found, i.e., related to changes on time scales of weeks and months or even years. Bagenal *et al.* [2015] found that the plasma density near Europa underwent long-term variations over the ~5 years of the Galileo orbiter. The density measurements are best fitted by different hot and cold populations [Bagenal *et al.*, 2015], where lower temperatures indicate that the plasma is more confined to the plasma sheet and thus imply a smaller vertical scale height. Such long-term variations could explain the brightness changes between the visits. For example, during flybys E11 and in particular E12, exceptionally high electron densities outside the expected variations were measured by Galileo [Kurth *et al.*, 2001] that could cause stronger auroral emissions at such times (or even weaker aurora depending on the exact effect of such high plasma densities on the atmosphere and electrodynamic interaction).

The slightly brighter emissions around the plasma sheet crossing at 110° than at 290° is also likely caused by asymmetries of the plasma sheet and of the magnetic field. The plasma sheet density is not azimuthally symmetric like assumed here. The magnetic field magnitude is slightly higher at the plasma sheet crossing near 110° than around 290° in both the VIP4 and VIPAL models, which also affects the electrodynamic interaction and thus aurora generation.

This magnetic field asymmetry is expected to induce a slightly higher total interaction strength and thus also a higher energy flux away from Europa through the Alfvén wings near 110° [Saur *et al.*, 2013, Figure 8], because more electromagnetic field and electron energy is transmitted onto Europa’s atmosphere and ionosphere. This also generates a higher energy flux being radiated away from Europa, which is expected to be coupled to the brightness of the auroral footprint of Europa in Jupiter’s ionosphere. The relative strength of the moon interaction can be characterized by the ratio of ionospheric electric field, E_i , to the corotational electric field, E_0 , or

$$\bar{\alpha} = 1 - \frac{E_i}{E_0} = 1 - \frac{2\Sigma_A}{\sqrt{\Sigma_H^2 + (\Sigma_P + 2\Sigma_A)^2}}, \quad (3)$$

[e.g., Saur *et al.*, 1999] with the ionospheric Hall and Pedersen conductances Σ_H and Σ_P and the Alfvén conductance Σ_A . $\bar{\alpha}$ is a measure for the relative strength of the interaction, with $\bar{\alpha} = 0$ corresponding to no interaction, and $\bar{\alpha} = 1$ to maximum relative interaction strength. For Europa the relative interaction strength is estimated to be about $\bar{\alpha} = 0.8$ [Saur *et al.*, 1998].

If the magnetic field strength increases, the relative interaction strength slightly decreases because Σ_A decreases. The physical reason is that a stronger magnetic field “stiffens” the flow, which is consequently less perturbed by Europa’s atmosphere. As a result, slightly less electrons are redirected around Europa’s atmosphere but are being convected into it. This results in a brighter auroral emission from Europa’s atmosphere.

If the magnetic field strength at Europa increases, the electromagnetic energy flux, i.e., the Poynting flux, radiated away from Europa also increases. The Poynting flux for small Alfvén Mach numbers ($M_A = 0.11$ at Europa for strong magnetic field) is proportional to $(\bar{\alpha}M_AB_0)^2 v_A$, with M_A the Alfvén Mach number, B_0 the background magnetic field, and v_A the Alfvén velocity [see Saur *et al.*, 2013, equation (55)]. This expression is approximately proportional to B_0 neglecting the small $\bar{\alpha}$ variability. For increasing B , this results in a larger energy flux toward Jupiter, which contributes to brighter auroral footprints. This physical dependence might be pictured with magnetic energy proportional to $(\bar{\alpha}M_AB_0)^2$ being radiated away with larger Alfvén velocities v_A for larger B_0 .

The maximum Europa footprint brightness was indeed measured near $\sim 110^\circ$, but the limited published footprint measurements do not allow to investigate systematic behavior [Wannawichian *et al.*, 2010]. Measurements of the correlation between the local aurora and footprint brightness would allow to establish how much of the footprint brightness is directly controlled by Europa’s local plasma and what are the contributions of wave propagation and particle acceleration along the Alfvén wing path to Jupiter.

4.1.2. Brightness at Different Orbital Longitudes

Next we investigate brightness trends as a function of Europa’s orbital position. Besides a slightly lower OI 1304 Å emission on the leading than on the trailing hemisphere (Figure 6a and section 3.1.1), we do not find systematic brightness variations related to the observing geometry or between the upstream and downstream sides of Europa in terms of the plasma flow. This suggests that the atmosphere is global in nature without any extreme density gradients between the hemispheres and that the electrons in the downstream region of Europa are not completely cooled down from collisions with neutrals. The very similar OII 1356 Å brightness at eastern and western elongation also suggests a rather azimuthally symmetric plasma density with respect to local time of Jupiter’s magnetosphere. A pronounced plasma sheet asymmetry between the dawnside (eastern elongation or leading hemisphere observations) and duskside (western elongation or trailing hemisphere) of Jupiter would likely cause differences in aurora brightness. The UV aurora brightness at Io, for comparison, was shown to be proportional to the ambient plasma density from a local time-dependent empirical model for the plasma torus [Smyth *et al.*, 2011] and thus is affected by dawn-dusk asymmetry of the Io plasma torus [Roth *et al.*, 2014c]. However, due to the geometry constraints for HST observations, namely, that the solar phase angle is always small ($< 11^\circ$), effects of local time and the plasma flow cannot be separated.

4.1.3. Global Morphology and Plasma Interaction

Overall, the morphology of Europa’s oxygen aurora appears to be distinctly different from the oxygen aurora at the neighboring Galilean moons Io and Ganymede. Ganymede’s aurora is shaped by the moon’s minimagnetosphere to form two ovals, and the lack of an intrinsic field at Europa leads to a substantially different interaction of the magnetospheric electrons with the atmosphere and explains the absence of auroral ovals.

The difference with Io's UV aurora morphology can not be explained so easily. While Io's aurora is clearly dominated by bright spots that are located roughly at the tangent points of the ambient magnetic field to the surface near the equator [Roesler et al., 1999; Retherford et al., 2000; Geissler et al., 2001], Europa's aurora is brightest around the magnetic poles as defined in section 3.2 and rather faint near the location where the spots arise at Io. Thus, there appears to be a general difference in the interaction of the plasma with the atmosphere that leads to the different aurora morphology.

The dimensionless parameters of the ambient plasma characterizing plasma-satellite interactions like the Alfvén Mach number and the plasma beta are similar in the environment of Io and Europa [Saur et al., 1998, 1999]. The atmospheric density is, however, about 2 orders of magnitude higher at Io [e.g., McGrath et al., 2004] leading to higher ionospheric densities and conductances. The higher ionospheric conductances cause a stronger reduction of the corotational electric field in the ionosphere, i.e., a higher $\bar{\alpha}$ after equation (3). The interaction parameter also describes the fraction of the upstream electrons that is diverted around the satellite's atmosphere: A higher $\bar{\alpha}$ means that relatively less electrons enter the atmosphere to potentially excite aurora.

Based on the conductances at Io, the interaction parameter is roughly $\bar{\alpha} = 0.9$ [Saur et al., 1999]. The development of Io's bright equatorial spots is explained by the diversion of the incoming plasma flow around large parts of the body [Saur et al., 2000]. Only at the flanks, the streamlines are less divergent, i.e., not directed toward or away from Europa, and more hot electrons are convected into the atmosphere to create the bright spots. Europa's conductances yield a weaker interaction with $\bar{\alpha} \approx 0.8$ [Saur et al., 1998]. A relatively large fraction of the incoming plasma can thus reach the areas near the magnetic poles on less divergent streamlines transporting relatively more hot electrons into this area.

Accordingly, Saur and Strobel [2004] find that Io's equatorial spots cease to be brighter than the global limb glow for neutral column densities around $(3-5) \times 10^{14} \text{ cm}^{-2}$, similar to the Europa's column density. A simulated oxygen aurora image for Europa from the same numerical model used by Saur and Strobel [2004] but applied for Europa by Saur et al. [1998] is displayed in Figure 19.10 of McGrath et al. [2004]. No pronounced equatorial spots are present for the assumed O_2 column density of $5 \times 10^{14} \text{ cm}^{-2}$, but a global limb glow with slight enhancements near the equator. The thin limb glow in the simulation image shown in McGrath et al. [2004] will be considerably spread over larger areas by the point spread function of the instrument, and a north-south brightness asymmetry due to differing electron energy reservoirs above and below Europa can lead to a fainter (and sometimes not visible depending on the color scale) emission on one hemisphere. Thus, Europa's aurora morphology could reflect a widespread half-limb glow around the northern or southern hemisphere in some of the images.

However, the observed morphology in most images appears more patchy and unstructured than such a limb glow and the brightest emissions are often found on the disk rather than right at or near the limb. Moreover, the area near the tangent points of the magnetic field lines at the flanks of Europa is fainter than the magnetic poles as shown in Figures 7a and 7b. Such a decrease of aurora excitation in this area is not expected for the symmetric interaction scenario as assumed in the model of Saur et al. [1998]. A possible mechanism that additionally perturbs the plasma flow, in particular, near the equatorial region, is the induced magnetic fields in the interior, which are strongest near the equator as the primary inducing field varies mostly in the equatorial plane. The induced fields were shown to deform the plasma flow at Europa such that the high ionospheric density regions on the flanks are more extended and shifted relative to the magnetic equator [see Schilling et al., 2008, Figure 6]. Now if at Europa the induction in a water ocean considerably perturbs the ionosphere near the equator, it might reduce or shift the aurora excitation and suppress the formation of equatorial spots. However, it needs to be shown quantitatively with numerical simulations, if the magnetic induction indeed leads to a decreased brightness of the aurora near Europa's magnetic equators. For Ganymede, measurable effects of the ocean on the aurora were recently shown in HST observations: The magnetic induction in the interior ocean reduces the oscillation of the moon's auroral ovals from $\sim 6^\circ$ to $\sim 2^\circ$ [Saur et al., 2015].

4.2. Atmosphere Properties

In this section, we first derive relative abundances for O to O_2 assuming homogeneous and constant electron properties and optically thin neutral column densities. The derived O/ O_2 ratios are independent of the highly variable plasma density. Thereafter, we apply a previously used [Hall et al., 1995, 1998; Saur et al., 2011] simple

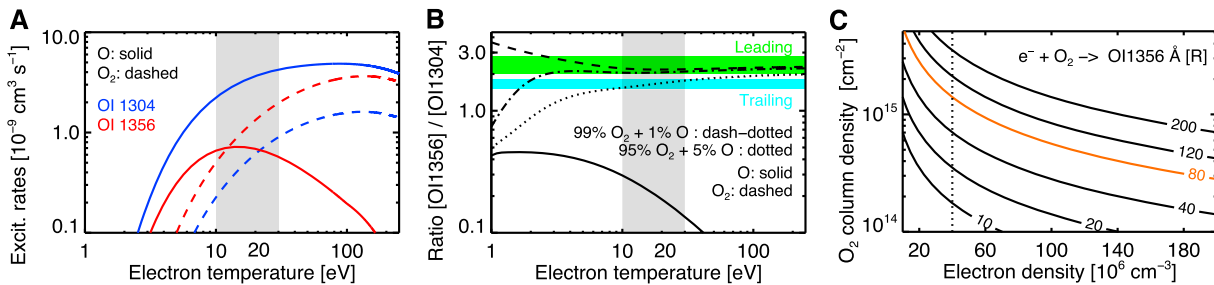


Figure 12. (a) Direct and dissociative excitation rates for O and O₂ producing OI 1304 Å and OI 1356 Å. (b) Oxygen line ratios of O/O₂ atmospheres. (c) OI 1356 Å brightness in R from excitation of O₂ as function of electron density and line-of-sight column density assuming two electron populations at 20 eV and 250 eV, see text. The grey shaded area in Figures 12a and 12b shows the temperature range of the cold plasma sheet electrons [Bagenal et al., 2015], the vertical dotted line in Figure 12c indicates the electron density often used to derive neutral abundances [Hall et al., 1995, 1998]. The shaded green and blue areas in Figure 12c show the range of measured oxygen ratios on the leading and trailing hemisphere, respectively (with one exception on each hemisphere outside the range but not displayed). The mean OI 1356 Å brightness of ~80 R is shown in orange (Figure 12c).

approach for a rough conversion of surface brightness to the product of electron density and neutral column density. Principally, several processes contribute to the emissions near Europa: electron excitation of molecular and atomic oxygen and, only for OI 1304 Å, solar resonance fluorescence scattering by O atoms [e.g., McGrath et al., 2009]. Contributions from resonant scattering will be small and neglected for most of our estimations to allow a derivation of O mixing ratios from just electron impact without knowledge of the absolute abundances. For reference, at a line-of-sight O column density of $5 \times 10^{12} \text{ cm}^{-2}$ and neutral temperature $T=150 \text{ K}$, resonantly scattered OI 1304 Å sunlight of ~4 R is expected. For electron-excited emission, the conversion of aurora brightness to absolute neutral abundances is always dependent on the density and temperature of the exciting electrons, which is however not known at the time of the observations. At the end of the section, we discuss possible atmospheric inhomogeneities related to the detected oxygen aurora morphology.

4.2.1. Atmospheric Oxygen Mixing Ratio

Oxygen line ratios of the total OI 1356 Å to OI 1304 Å brightness between 1.5 and 2.8 were derived, with higher values on the leading side and lower values on the trailing hemisphere. A similar difference was measured by Hall et al. [1998] (see their Table 1), although their uncertainties were larger than the difference. There are two effects that can cause such a hemispherical difference in the atmospheric oxygen emissions: (1) variations in atmospheric composition from the leading to the trailing hemisphere and (2) variations of the temperature of the exciting electrons leading to changing relative excitation of the two oxygen lines.

Figure 12a shows electron impact excitation rates derived from the experimentally determined cross sections for excitation of O [Doering and Gulcicek, 1989a, 1989b; Doering, 1992] and dissociative excitation of O₂ [Kanik et al., 2003] assuming Maxwellian electron energy distributions. The thermal electrons at Europa have a core temperature from 10 to 30 eV with a ~5% suprathermal tail with a temperature >200 eV [Sittler and Strobel, 1987; Bagenal et al., 2015]. Electron dissociative excitation of O₂ is the only viable process to generate the observed oxygen brightness of several tens of Rayleighs and simultaneously the oxygen ratio of ~2 through excitation by the magnetospheric plasma at Europa [e.g., Hall et al., 1998; Roth et al., 2014a] (Figure 12b). Excitation of O produces significantly more OI 1304 Å emission (solid, Figure 12b) at all electron temperatures. In case of an optically thick O column, the detected OI 1304 Å emissions can be reduced relative to the unaffected optically thin OI 1356 Å emission. However, resonantly scattered sunlight will additionally contribute at 1304 Å but not at 1356 Å, and the additional scattered OI 1304 Å brightness precludes 1356/1304 ratios well above 1. Excitation of other species such as H₂O or OH also produce more OI 1304 Å emission and are negligible for the abundances expected for the global atmosphere [e.g., Shematovich et al., 2005; Smyth and Marconi, 2006; Roth et al., 2014a]. The 1356/1304 ratio increases for both O and O₂ toward lower temperatures. Thus, a line ratio increase from upstream to downstream can be explained by either a decrease of the O mixing ratio or a temperature change, or both.

We now analyze the measured oxygen ratio with regard to the atmospheric O and O₂ abundance and focus thereby on the thermal electrons, since they contribute about 90% to the total excitation for the generally assumed mixing ratio of 5% suprathermal electrons. The ratios measured on the trailing side lie between the ratios expected for purely O and O₂ atmospheres (Figure 12). Assuming that the thermal plasma on the

upstream hemisphere was not significantly cooled from collisions and thus has an electron temperature of 20 eV, the mean oxygen line ratio on the trailing side of 1.6 is best explained by a mixing ratio of 5% O, see dotted line in Figure 12.

On the downstream side, the electrons are on average cooled down through collisions in the atmosphere. Model calculations of *Saur et al.* [1998] find a decrease from an assumed upstream temperature of 20 eV down to 10–15 eV. Now on the leading or downstream side almost consistently higher line ratios between 2.0 and 2.8 are measured (with one exception). The theoretical 1356/1304 ratios from the excitation of either O (Figure 12b, solid) or O₂ (dashed) increase with decreasing temperature from 20 eV to ~10 eV. Thus, the higher downstream values might be related to the lower electron temperature in the downstream region, if the atmosphere consists of only O or O₂. For a mixed atmosphere, however, excitation of O becomes relatively more important compared to O₂ toward lower temperatures (Figure 12a) and therefore the 1356/1304 ratio for a mixing ratio of 5% O to O₂ overall decreases, as direct excitation of O produces more OI 1304 Å at all temperatures. To match the leading side ratios greater than two, an oxygen mixing ratio of less than 1% is required (Figure 12b, dash-dotted line).

For such a low O mixing ratio of only ~1%, however, the measured trailing side ratios are inconsistent with the theoretical 1356/1304 ratios at all temperatures. In other words, it is not possible to explain the leading-trailing difference by only a difference in electron temperature based on the adopted excitation rates. Instead, the line ratio difference suggests a compositional change with less atomic oxygen on the leading or downstream side of Europa. Atomic oxygen, O, is produced from dissociation of O₂ by primarily electron impact (and by solar UV radiation) with excess kinetic energies causing escape of the O atoms from Europa. Its residence time is more than an order of magnitude lower than that of O₂ [*Smyth and Marconi*, 2006]. Thus, the inferred depression of atomic oxygen on the leading side is consistent with a reduced electron impact production in the cold wake region. The temperature drop from the upstream to the downstream side might therefore directly affect the 1356/1304 ratio through the temperature-dependent excitation rates and also indirectly through the production of O from O₂ by impact dissociation. The simulations of *Saur et al.* [1998] suggest a decrease from 20 eV upstream down to 10 eV in the near wake, and the rates for dissociation and dissociative excitation for OI 1304 Å decrease by a factor of ~3 over this temperature range (Figure 12) [*Cosby*, 1993].

4.2.2. Coronal Oxygen Mixing Ratio

Our observed decrease of the 1356/1304 ratio with altitude above the disk implies higher mixing ratios of atomic oxygen in the corona in agreement with measurements of atomic oxygen as dominant species at larger distances from Europa [*Hansen et al.*, 2005]. Table 2 summarizes the ratio ranges for the derived oxygen ratios in two regions above 1.25 R_E for electron excitation only. Note that at altitudes of >1.5 R_E the derived O column density corresponds to >1/4 of the O₂ column density, but O₂ prevails up to the edges of the STIS images.

The lower brightness of <15 R above 1.25 R_E from the disk center for both lines imply lower oxygen column densities and thus a lower optical depth. However, solar fluorescence might contribute a few Rayleighs to OI 1304 Å. The O mixing ratios in Table 2 can therefore be considered upper limits, since backscattered sunlight as additional OI 1304 Å source would reduce the amount of O needed to reproduce the coronal 1356/1304 ratios. Because of the low absolute brightness and low SNRs in the corona, the derived corona ratios vary significantly for the individual visits and we refrain from analyzing or interpreting these individual ratios here.

4.2.3. Oxygen Column Densities

We will now use the OI 1356 Å brightness as proxy to derive abundances of the dominant species of the near-surface atmosphere, O₂, not taking into account emission contributions from O. Following the approach of *Hall et al.* [1995, 1998] and *Roth et al.* [2014a], we further use the very simplifying assumption of constant homogeneous plasma parameters to convert the OI 1356 Å brightness to a line-of-sight O₂ column density. In accordance with the previous studies we assume two Maxwellian-distributed electron populations: a thermal core with $k_B T_e = 20$ eV plus a suprathermal population with $k_B T_e = 250$ eV and fixed mixing ratio of 5%.

While the OI 1304 Å brightness strongly depends on the atomic to molecular oxygen mixing ratio and is less suited to derive absolute neutral abundances, excitation of O₂ will contribute >95% of the OI 1356 Å emission for any O atom mixing ratios of <10% at the assumed temperatures, see also Figure 12a. Thus, the OI 1356 Å brightness depends predominantly on the O₂ abundance.

In the previous approximations a plasma density of 40 cm^{-3} was used based on Voyager measurements [Sittler and Strobel, 1987], but Galileo observations suggest higher plasma densities near Europa [Kurth *et al.*, 2001; Bagenal *et al.*, 2015]. Because of this uncertainty and the variability of the electron density with Jupiter's rotation, it is difficult to derive absolute neutral abundances as the aurora brightness rather reflects the product of electron and neutral density. Figure 12c shows the theoretical O_{II} 1356 Å brightness for various atmospheric and plasma densities. For the canonical electron density value of 40 cm^{-3} the overall average O_{II} 1356 Å brightness of $\sim 80 R$ converts to a O₂ column density of $1.4 \times 10^{15} \text{ cm}^{-2}$, but a fivefold higher electron density measured, for example, during Galileo flyby E15 [Bagenal *et al.*, 2015] naturally requires a 5 times lower O₂ column density of $2.8 \times 10^{14} \text{ cm}^{-2}$.

Note that the derived column densities can be converted to total O₂ abundances that relate to the total measured brightness by multiplying the column density with the area of Europa's disk, since we have normalized the total brightness to moon disk in the beginning. To derive abundances from surface brightness, our "total brightness" values need to be corrected by a factor of $1/(1.25)^2$ (see section 3.1) and the O_{II} 1356 Å surface brightness within $1.25 R_E$ equals $80 R/(1.25)^2 = 51R$ and the column density for an electron density of 40 cm^{-3} becomes $9 \times 10^{14} \text{ cm}^{-2}$. At higher altitudes between 1.25 and $1.5 R_E$, the O_{II} 1356 Å surface brightness drops down to $\sim 12 R$, which converts to a line-of-sight O₂ column density of $2 \times 10^{14} \text{ cm}^{-2}$ (again neglecting contributions from O).

Our results are similar to previously derived O₂ abundances based on the similarly measured brightness [Hall *et al.*, 1995, 1998; Saur *et al.*, 2011]. However, we remind the reader that our analysis has revealed that the aurora is strongly controlled by the time variable and inhomogeneous plasma environment and moon-magnetosphere interaction, and this approach is only a very crude approximation of the neutral gas abundance to generate the aurora. A self-consistent calculation of the electron temperature and density is crucial to correctly reproduce the aurora generation and to derive conclusion about atmospheric abundances. The simulation by Saur *et al.* [1998] includes such self-consistent electron treatment and reveals that slightly lower O₂ abundances might be sufficient to generate the measured brightness, rather than the estimated, with the simple approach above.

Overall, several aspects point to the lower end of the generally derived and assumed range of 2×10^{14} to $1.5 \times 10^{15} \text{ cm}^{-2}$ [cf. Hall *et al.*, 1995, 1998; Saur *et al.*, 1998; Schilling *et al.*, 2008; Saur *et al.*, 2011; Rubin *et al.*, 2015, this study]: First, the values higher than $1 \times 10^{15} \text{ cm}^{-2}$ in the literature are derived assuming a magnetospheric electron density of 40 cm^{-3} based on the Voyager measurements, but up to 5 times higher densities were frequently measured by Galileo near Europa, which necessitate lower atmospheric densities. Second, the self-consistent model of Saur *et al.* [1998] reveals that the oxygen brightness can be reproduced by a lower atmospheric column density than that derived with the simplifying approach of Hall *et al.* [1995], which is also applied here. Third, the eclipse images suggest an optically thin O column density ($\tau \lesssim 1$), which thus needs to be lower than $3 \times 10^{12} \text{ cm}^{-2}$ assuming a O temperature of 150 K. Taking the derived O mixing ratios of $\sim 3\%$ on average for the leading and trailing near-surface atmosphere, this O column in turn implies an O₂ column density on the order of 10^{14} cm^{-2} rather than 10^{15} cm^{-2} . Fourth, the lack of equatorial spots is another hint for a low-density atmosphere, as more pronounced spots are expected to form for higher atmospheric densities [Saur and Strobel, 2004]. And lastly, the normalization to Europa's disk center of the total flux, which is actually measured by summing over all pixels in a larger area of radius $1.25 R_E$, generally leads to an overestimation of the line-of-sight column (which is also reflected by the second point).

Recently, Shemansky *et al.* [2014] disputed the interpretation of Europa's oxygen emissions as due principally to electron impact dissociative excitation of O₂ and argued instead that it is electron excitation of atomic oxygen with a column density approximately 2 orders of magnitude lower than the O₂ column densities derived in this study and inferred previously [e.g., Hall *et al.*, 1998]. There are several weaknesses in the argumentation by Shemansky *et al.* [2014], some of which we will point out here.

Their analysis is based on Cassini UVIS spectra, where the solid angle of Europa on the detector is about 50 times smaller than a pixel size, so it acts as a point source for the spectrograph. UVIS thus completely lacks the spatial resolution to isolate photons originating from the atmosphere of Europa rather than an extended corona/neutral cloud of O atoms possibly within the Hill sphere. Consequently, no conclusions can be reached about the near-surface atmosphere of Europa. Whereas the HST/STIS images have a spatial resolution between 71 km and 95 km (depending on Europa's distance) per pixel and it is thus possible to

differentiate between what originates from the atmosphere within ~ 500 km from the surface and on the disk from what originates from an extended corona as, e.g., discussed in section 4.2.3.

Furthermore, *Shemansky et al.* [2014] assumed that neutral O atoms have a temperature of $T=1000$ K, which yields for OI 1304 Å a line center cross section of 9×10^{-14} cm². With their inferred O column density of 4.7×10^{12} cm⁻² the optical depth is $\tau = 0.42$. This cannot be considered optically thick for an extended corona, nor is the optical depth sufficient to alter emission line ratios within the OI 1304 Å multiplet as shown in their Figure 6. Their assumed magnetospheric impacting electron density of $14,000$ cm⁻³ at a electron temperature of $k_B T_e = 7.5$ eV (cf. their Figure 6) corresponds to the maximum observed electron density and exceeds the average of the Galileo radio-occultation-measured ionospheric, *cold* electron densities [*Kliore et al.*, 1997]. Resonance scattering of the solar OI 1304 Å multiplet with their inferred column density yields approximately $2.5 R$.

Therefore, the O column density inferred in *Shemansky et al.* [2014] can neither produce the absolute oxygen brightness when using appropriate and reasonable electron properties, nor can a pure atomic oxygen atmosphere reproduce oxygen 1356/1304 ratios higher than 1.5 (and up to 2.8) as accurately derived for Europa's near-surface atmosphere in this study.

Whereas Europa O₂ may be lost directly by charge exchange producing fast neutrals that leave the Jovian system, most of the O₂ is lost (1) by stripping ionospheric O₂⁺ by $\vec{E} \times \vec{B}$ convection followed by recombination to hot O atoms and (2) by thermal ion atmospheric sputtering (knock-on collisions) that dissociate O₂ and impart most momentum to one nucleus [e.g., *Dols et al.*, 2015], which escapes leaving behind an O atom to escape thermally. Thus, Europa's extended corona will be preferentially populated by O rather O₂, and a considerable fraction of escaping O and O₂ will have speeds in excess of Jupiter's escape velocity. Our analysis of the HST/STIS images yields such an atmosphere of O₂ transitioning to an O atom corona in sharp contrast to the misinterpretation of the extremely low spatial resolution UVIS data by *Shemansky et al.* [2014]. *Shemansky et al.* [2014] also misinterpret the previous STIS data presented in *Roth et al.* [2014a] by deriving brightness values for the two oxygen multiplets from larger spatial regions instead of taking into account only pixels near Europa (for which values are given in Table S1 of *Roth et al.* [2014a]). In that way they yield oxygen line ratios for the STIS data that do not at all represent the near-surface atmosphere but match their proposed theoretical ratios.

4.2.4. Neutral Gas Scale Height

A basic characteristic of an atmosphere is the scale height. The spatial aurora profiles measured above the limb might reflect the density profiles to some extent if the spatial variations of the electron temperature and density are small compared to neutral gas gradient. The limb profiles as measured in the images are also significantly affected by the overlap of the individual images of the multiplet lines that are offset on the detector and by the instrument point spread function (PSF) (see also Supplementary Material of *Roth et al.* [2014a]), and it is thus not possible to directly analyze the derived spatial profiles.

To account for the instrument effects, we generate theoretical limb profiles by simulating images for a globally uniform density at the surface (as proxy for local volume emission rate) that decreases exponentially with altitude h with a certain scale height H , i.e., following $e^{-h/H}$. By integrating along a line of sight through such a radially symmetric atmosphere, images of the line-of-sight-integrated fluxes are generated. Separate images are then generated for each line of the OI 1304 Å and OI 1356 Å multiplets, weighted with the theoretical relative intensity of the lines and superposed to generate artificial OI 1304 Å and OI 1356 Å detector images. The images are scaled to the average resolution of the STIS images and convolved with the STIS PSF. Finally, we extract radial brightness profiles by averaging over all pixels in concentric rings from the center to 1000 km above the surface like we did for the observation images. With this approach we are able to reproduce the instrument-related effects on the spatial profiles in the images.

Figures 11b and 11c show the profiles extracted from modeled OI 1356 Å and OI 1304 Å images for scale heights of 50 km, 150 km, and 300 km in comparison to the superposed profile from all the respective STIS observation images. The modeled profiles $I_{\text{limb}}^{\text{mod}}(r)$ are functions of the radial distance and are fitted to the observed profiles $I_{\text{limb}}^{\text{obs}}(r)$ above the limb (i.e., for all $r > R_E$ with a linear function of the form $a I_{\text{limb}}^{\text{mod}}(r) + b$ to account for the arbitrary scaling of the model (with parameter a) and offset from zero (parameter b) that could reflect a constant background brightness from an extended tenuous corona at Europa.

It is obvious from Figures 11b and 11c that above the limb (only data points $r > R_E$) the profile of the lowest scale height of 50 km is a worse fit to the data than the model profiles with larger scale heights. Both the $H=150$ km and $H=300$ km profiles reproduce the observed OI 1304 Å profile well and the derived chi-square values for the fits of 0.8 and 0.6, respectively, favor the larger scale height. For OI 1356 Å, the fitted model profiles agree less with the measured profile with chi-square values of 3.5 and 3.6 for $H=150$ km and $H=300$ km, respectively, slightly favoring the smaller scale height of the two. Hence, for both emissions larger scale heights are favored, but an accurate determination of the scale height is hampered by the strong influence of the PSF and the overlapping multiplet lines.

None of the profiles that were fitted above the limb is consistent with the measured brightness profile on the disk, but all underestimate on-disk brightness consistently. Generally, lower scale heights, i.e., the emissions that are confined to very low altitudes, would be required to reproduce the relatively high emissions on the disk compared to the lower detected above-limb emissions. However, low scale heights should lead to a strong brightness peak right at the limb, which is not observed. This mismatch of the fitted profiles indicates that the aurora distribution is not globally symmetric as assumed in our model images likely because the electron density and temperature are not radially symmetric.

Applying again the simplifying assumption of a spatially homogeneous electron excitation, we shortly discuss the possible relation to the atmospheric profiles. The best fit scale height of 150 km for OI 1356 Å is similar to the O₂ scale height estimated by *Saur et al.* [1998] based on one-dimensional calculations of a vertical atmospheric temperature profile. As discussed above, the OI 1356 Å emissions will mostly reflect the O₂ abundance and be less affected by the atomic oxygen. The OI 1304 Å brightness, in contrast, can originate to large extents from atomic oxygen at higher altitudes, where the total brightness is on the order of only a few Rayleighs and the line ratio drops below 1, see Figure 11a and Table 2. A 2 times larger scale height is generally expected for the lighter atomic oxygen than for O₂ in thermal equilibrium, which might explain the shallower profile of the OI 1304 Å line and the decreasing 1356/1304 ratio. However, it is important to remember that the derived emission scale height will not reflect the scale height of the neutral density, as the aurora was demonstrated to be strongly affected by the inhomogeneous plasma density and temperature.

For example, the interaction of the plasma with the atmosphere will lead to a considerable electron temperature decrease near the surface as shown by *Saur et al.* [1998] and more recently in the simulation of *Rubin et al.* [2015]. Therefore, the aurora profile does not reflect the radial profile of the atmosphere, as the auroral profile is the convolution of the effects of the electron distribution function and the neutral density. For example, a temperature drop down to 10% of the initial upstream temperature or lower close to the surface as seen in the model of *Rubin et al.* [2015] might reduce the aurora excitation by a similar portion (assuming a linear dependency of excitation rate to the temperature) and will severely modify the measured emission profile. We hence note again that a self-consistent simulation of the plasma interaction for various atmospheric scale heights is needed to determine the relation of the aurora profile to the atmospheric profile.

4.2.5. Density Inhomogeneities

The inferred strong influence of the time-variable-perturbed plasma environment on the aurora morphology complicates the inference of reliable information on the atmospheric distribution. For example, previous studies concluded or assumed an atmospheric surplus in the northern anti-Jovian quadrant on the trailing hemisphere based on the aurora surplus in the 1999 STIS images [*Cassidy et al.*, 2007; *Plainaki et al.*, 2013]. However, the detected emission morphology can be explained by Europa's position below the plasma sheet and the orientation of the magnetic field during four of the five HST orbits of the 1999 visit, and an atmospheric inhomogeneity is not required or indicated. Another inhomogeneous morphology with a local surplus in the left northern quadrant was observed in images of visible emissions in eclipse (which were assigned to Na) by Cassini ISS [*Cassidy et al.*, 2008]. A closer look at the average magnetic field orientation during the Cassini exposures shows that the emission surplus coincides roughly with the magnetic pole and is thus likely consistent with the magnetospheric-induced morphology seen in the STIS eclipse images. Plasma effects, similarly, can explain an oxygen FUV aurora surplus near 90° west longitude detected in HST Advanced Camera for Surveys (ACS) observations [*Saur et al.*, 2011]. One of several possibilities for the origin of this anomaly was discussed by the authors to be a plume, but the anomaly fits well into the aurora morphology patterns reported here, i.e., brighter emission near the poles and fainter areas at the flanks of Europa most likely caused by the plasma interaction.

4.3. Other Detected Aurora Characteristics

In this section, derived characteristics that could not be unambiguously assigned to either plasma or atmospheric effects are discussed.

4.3.1. Long-Term Change Between 1999 and 2012–2015 Period

The cause for the systematic deviation of the brightness during visit 1 in October 1999 can in principal originate from a change in either Europa's atmosphere or the ambient magnetosphere between 1999 and the 2012–2015 era of all other measurements.

Because there is no independent measurement of the atmospheric density, a change of the global neutral gas abundance as a possible cause can not be assessed but is theoretically possible.

Significant long-term changes of the magnetospheric plasma density structure were derived by *Smyth et al.* [2011] for three epochs (1979, 1991, and 1995) from Voyager, Galileo, and ground-based data. We could show that the aurora brightness roughly scales with the changes in plasma density at different System III longitudes. Assuming that the atmosphere is stable and that the brightness is proportional to the plasma density, the ~50% lower auroral emissions in the 2012–2015 era would imply a systematically lower plasma density in Europa's orbit by a similar factor.

There is only one small technical difference in the early observations, as the target was vertically centered in the slit and on the detector in 1999, while it is located at the bottom of the slit after 2012 because of the high detector noise in the upper detector part that has developed over the years. However, this should not lead to systematic brightness differences as the detector sensitivities are accounted for in the processing.

4.3.2. Left-Right Aurora Asymmetry

Brighter emissions were found on the right hemisphere in almost all images with an average emission surplus of >50% compared to the left hemisphere. One explanation for the consistent left-right asymmetry are atmospheric changes with local time on Europa, as the brighter right hemisphere always coincides the afternoon or dusk hemisphere and the fainter hemisphere is the morning side. Variations of the oxygen abundance from dawn to dusk could arise from surface temperature changes with local time. A temperature difference between Europa's dayside (~130 K) and nightside (~90 K) was measured by the Galileo Photopolarimeter-Radiometer (PPR) [Spencer et al., 1999]. Such a day-night difference suggests a thermal inertia of the surface that in turn should lead to higher afternoon temperatures, which was indeed found for individual locations in the PPR data [Rathbun et al., 2010]. If a morning-afternoon temperature gradient is globally present, it can cause differing sputtering yields [Famá et al., 2008; Plainaki et al., 2013]. However, the temperature dependence of the sputtering yields and particularly the effects on local abundances need further study to show whether it can explain a >50% brighter aurora on the afternoon or dusk hemisphere compared to the morning or dawn hemisphere. The reactivity of O₂ with Europa's porous regolith surface (which is generally very low and often assumed to be zero) as atmospheric sink could additionally generate an atmospheric inhomogeneity [Cassidy et al., 2007], but a temperature-dependent change of the reactivity is not known.

Plasma physical effects can also cause an asymmetric plasma flow (e.g., by the ionospheric Hall effect) and thus aurora asymmetries. How the details of the various nonlinear effects interact is difficult to predict without appropriate numerical models, but it is important to keep in mind that the derived dusk/dawn asymmetry is not necessarily related to local time effects.

4.4. Implications From Eclipse Observations

The fact that the aurora brightness does not change much in eclipse has several implications for Europa's atmosphere: First, the global neutral density is rather independent of sunlight as expected for Europa's predominantly sputtering-generated atmosphere. And second, that the optical depth of the atomic O column to OI 1304 Å is relatively low, since resonantly scattered OI 1304 Å emission should lead to a higher OI 1304 Å brightness in sunlight than in eclipse for an optically thick O atmosphere (resonant scattering is negligible for the semiforbidden OI 1356 Å line in any case). This is in agreement with previously derived atmospheric O abundances at Europa [Hall et al., 1995, 1998]. Furthermore, the unchanged 1356/1304 ratio in eclipse also suggests that photodissociation of O₂ to produce O plays a minor role compared to electron impact dissociation. Otherwise an increased 1356/1304 ratio from a lower O abundance in eclipse would be expected. The importance of electron impact dissociation is further supported by the difference in O mixing ratio that we found on the leading and trailing hemisphere, which is best explained by the cooling of the

impacting electrons from upstream to downstream. This finding would then contradict the results from the kinetic model of *Shematovich et al.* [2005] that photodissociation is the main loss for the atmospheric O₂.

The STIS images analyzed here were the first spectrally resolved observations of Europa's UV emissions in eclipse of Jupiter. Previous images taken in eclipse by HST/ACS [*Retherford et al.*, 2007] are difficult to interpret, because Europa's location can not be determined unambiguously and reference ACS observations with identical setup in sunlight are not available for comparisons. Hence, our observations provided the first published and reliable results on the oxygen line ratio and oxygen aurora morphology of Europa in eclipse, including the direct comparison to the aurora before ingress and after egress.

5. Summary and Conclusion

We have analyzed the oxygen OI] 1356 Å and OI 1304 Å emissions in a large, comprehensive set of HST/STIS spectral UV images of Europa. The images were taken during 20 HST visits in October 1999 and between January 2014 and April 2015. On five occasions Europa was eclipsed by Jupiter during the entire or parts of the visit providing the first spectral UV images in eclipse. The images are taken at various orbital longitudes providing views on all sides of Europa. The detector images are processed through a pipeline including a correction for background emissions and sunlight reflected off the surface. Thereby, FUV albedos in a wavelength range between 1430 Å and 1530 Å are derived. We find slightly higher values on the leading than on the trailing hemisphere, in accordance with the much stronger albedo dichotomy at visible wavelengths that is thought to be caused by preferred particle bombardment of the trailing or upstream hemisphere.

The inferred oxygen brightness and morphologies of the OI] 1356 Å and OI 1304 Å emissions are very similar and are both strongly affected by the variable plasma environment. The aurora brightness systematically decreases with increasing distance of Europa to the plasma sheet center and the inferred vertical scale height for OI] 1356 Å is consistent with plasma sheet scale heights by *Bagenal and Delamere* [2011]. The brightest emissions are mostly concentrated near the magnetic poles, i.e., near the intersection of the unperturbed magnetic field line bisecting Europa and the moon disk. In images of the trailing or upstream side, the emissions are clearly brighter on the hemisphere that faces the plasma sheet center, showing a good correlation to the asymmetric electron energy content of the fluxtubes "above" and "below" Europa. Such a north-south asymmetry was previously detected for Io's limb glow [*Retherford et al.*, 2003; *Roth et al.*, 2014b].

At the flanks near the tangent points of the magnetic field to the disk, where Io's bright equatorial spots arise, Europa's oxygen emissions are faint. The lack of pronounced equatorial spots can be explained by the lower atmospheric densities at Europa compared to Io and a less divergent plasma flow [*Saur and Strobel*, 2004]. However, even for a thinner atmosphere the emissions near the flanks are expected to be as bright as the polar emissions for a globally symmetric atmosphere, but not to be fainter as observed. Induced magnetic fields in a saline, electrically conductive ocean generated by the time variable component of the magnetospheric field at the location of Europa will also affect the aurora. The induction effects might reduce the brightness at the flanks through perturbations of the plasma flow [*Schilling et al.*, 2008], but self-consistent modeling that includes the interior induction is needed to investigate this further. In some images, the observed morphology can be described as a half-limb glow on the hemisphere facing the plasma sheet, which is severely broadened by instrument effects. However, Europa's aurora morphology appears highly variable and often patchy and the formation might be very sensitive to changes in the magnetospheric environment and the electrodynamic interaction.

The images taken in October 1999 reveal a systematically higher oxygen aurora brightness for both lines by ~50% compared to the 19 visits between 2012 and 2015, caused by a systematic change of either the plasma properties or the Europa's atmosphere (or both).

No changes in absolute brightness or in oxygen line ratio are detected in the eclipse images. The persistence of the aurora throughout eclipse indicates that both the atmosphere and aurora are not directly affected by sunlight. Hence, electron impact processes presumably prevail over photo processes in agreement with the results from *Saur et al.* [1998]. The mostly unchanged OI 1304 Å brightness suggests a low optical depth of the atomic oxygen column density. Sublimation as additional neutral gas source on the dayside is small.

Considering various aspects of the variable plasma environment and the atmospheric distribution, the detected oxygen brightness suggest line-of-sight O₂ column densities of $(3-6) \times 10^{14} \text{ cm}^{-2}$.

Differing 1356/1304 ratios of 1.6 (0.1) and 2.3 (0.3) on the trailing (or upstream) and leading (or downstream) sides in the near-surface atmosphere require different O mixing ratios of $\sim 5\%$ and $\lesssim 1\%$, respectively. Since the change of the oxygen line ratio is connected to a decrease in OI 1304 Å brightness from upstream to downstream (the OI 1356 Å brightness is similar on both sides), a lower O abundance downstream of Europa is the best explanation. The lower downstream O abundance can be caused by a drop in electron impact dissociation of O₂ due to the cooling of the plasma near Europa.

The average 1356/1304 ratio of ~ 2 in the near-surface region decreases with increasing altitude to values < 1 at distances $> 1.5 R_E$ to the disk center, and we derive upper limits of O mixing ratios for the corona (Table 2). The inferred higher relative O abundances in the corona are consistent with previous observations [Hansen *et al.*, 2005] and theoretical expectations [Shematovich *et al.*, 2005; Smyth and Marconi, 2006] of an extended O cloud, but O₂ is more abundant up to distances of $\sim 1.6 R_E$ from the disk center (or ~ 900 km above the surface) at the edges of our images.

We furthermore find that the aurora is almost consistently brighter on the right hemisphere at all orbital longitudes with a $> 50\%$ higher emissions on average than on the left hemisphere. This asymmetry can not be unambiguously assigned to obvious plasma effects or known atmospheric inhomogeneities but constitutes a significant and puzzling result that requires consideration in atmosphere and plasma simulation efforts. Vertical brightness profiles above limb indicate scale heights larger than 100 km for both the OI 1356 Å and OI 1304 Å emission decrease with altitude. A slightly slower decrease is found for OI 1304 Å in agreement with the more extended atomic O cloud that produces more OI 1304 Å than OI 1356 Å. However, the relation of the derived aurora profiles to the actual atmospheric altitude profiles is unclear and can be considerably masked by the distribution of the energetic electron density within the atmosphere.

Atmospheric inhomogeneities could not be derived from the oxygen aurora morphologies and some previous hints for inhomogeneities [Cassidy *et al.*, 2007; Saur *et al.*, 2011] are likely caused by the derived plasma effects on the aurora. The localized above-limb OI 1304 Å surplus coincident with a surplus in H Lyman α emission and detected in December 2012 [Roth *et al.*, 2014a] does not significantly change the global morphology, and therefore, neither affects the morphology parameters derived in this study (see, e.g., Figures 5 and 7). This shows that local inhomogeneities like the one detected in December 2012 and explained by a localized H₂O abundance, can hardly be identified in the time variable and patchy oxygen aurora images only, but can be detected only through the simultaneously obtained H Lyman α image. The processing and analysis of the Lyman α images a different in several aspects and will be published in a future paper.

The STIS images analyzed in this paper provide the most comprehensive and detailed data set on Europa's oxygen aurora and atmosphere up to date, and the derived aurora and atmosphere properties will be helpful to better understand Europa's atmosphere and its plasma interaction with Jupiter's magnetosphere in future theoretical or numerical studies. The three future and ongoing missions to the Jupiter system will deliver new UV aurora data with higher cadence and better spatial and spectral resolution to improve our picture of Europa's atmosphere. All three spacecraft, NASA's *Juno* and *Europa* missions as well as ESA's *Jupiter Icy moon Explorer* (JUICE), will carry an ultraviolet spectrograph on board.

Acknowledgments

This work is based on observations with the NASA/ESA Hubble Space Telescope obtained at the Space Telescope Science Institute, which is operated by the Association of Universities for Research in Astronomy (AURA), Inc., under NASA contract NAS 5-26555. The work at the Johns Hopkins University and Southwest Research Institute was supported by NASA grants HST-GO-13040.001-A and HST-GO-13679.002-A. L.R. appreciates the support from the Swedish VINNOVA agency and the Göran Gustafsson foundation. This study has been partially performed in the context of the activities of the ISSI International Team 322. The HST data used in this work are available on the MAST archive of STScI at <http://archive.stsci.edu>. Excellent comments by the anonymous referees are also acknowledged.

References

- Bagenal, F., and P. A. Delamere (2011), Flow of mass and energy in the magnetospheres of Jupiter and Saturn, *J. Geophys. Res.*, *116*, A05209, doi:10.1029/2010JA016294.
- Bagenal, F., E. Sidrow, R. J. Wilson, T. A. Cassidy, V. Dols, F. J. Cray, A. J. Steffl, P. A. Delamere, W. S. Kurth, and W. R. Paterson (2015), Plasma conditions at Europa's orbit, *Icarus*, *261*, 1–13, doi:10.1016/j.icarus.2015.07.036.
- Brown, M. E. (2001), Potassium in Europa's atmosphere, *Icarus*, *151*, 190–195, doi:10.1006/icar.2001.6612.
- Brown, M. E., and R. E. Hill (1996), Discovery of an extended sodium atmosphere around Europa, *Nature*, *380*, 229–231, doi:10.1038/380229a0.
- Brown, W. L., W. M. Augustyniak, E. Simmons, K. J. Marcantonio, L. J. Nazzerotti, R. E. Johnson, C. T. Reimann, G. Foti, and V. Pirronello (1982), Erosion and molecular formation in condensed gas films by electronic energy loss of fast ions, *Nucl. Instrum. Methods Phys. Res. A*, *198*, 1–8.
- Cassidy, T. A., R. E. Johnson, M. A. McGrath, M. C. Wong, and J. F. Cooper (2007), The spatial morphology of Europa's near-surface O₂ atmosphere, *Icarus*, *191*, 755–764, doi:10.1016/j.icarus.2007.04.033.
- Cassidy, T. A., R. E. Johnson, P. E. Geissler, and F. Leblanc (2008), Simulation of Na D emission near Europa during eclipse, *J. Geophys. Res.*, *113*, E02005, doi:10.1029/2007JE002955.
- Cassidy, T. A., C. P. Paranicas, J. H. Shirley, J. B. Dalton, B. D. T. III, R. E. Johnson, L. Kamp, and A. R. Hendrix (2013), Magnetospheric ion sputtering and water ice grain size at Europa, *Planet. Space Sci.*, *77*, 64–73, doi:10.1016/j.pss.2012.07.008.
- Connerney, J. E. P., M. H. Acuña, N. F. Ness, and T. Satoh (1998), New models of Jupiter's magnetic field constrained by the Io flux tube footprint, *J. Geophys. Res.*, *103*, 11,929–11,940, doi:10.1029/97JA03726.

- Cosby, P. C. (1993), Electron-impact dissociation of oxygen, *J. Chem. Phys.*, *98*, 9560–9569, doi:10.1063/1.464387.
- Doering, J. P. (1992), Absolute differential and integral electron excitation cross sections for atomic oxygen: IX. Improved cross section for the $^3P-^1D$ transition from 4.0 to 30 eV, *J. Geophys. Res.*, *97*, 19,531–19,534, doi:10.1029/92JA02007.
- Doering, J. P., and E. E. Gulcicek (1989a), Absolute differential and integral electron excitation cross sections for atomic oxygen: VII. The $^3P-^1D$ and $^3P-^1S$ transitions from 4.0 to 30 eV, *J. Geophys. Res.*, *94*, 1541–1546, doi:10.1029/JA094iA02p01541.
- Doering, J. P., and E. E. Gulcicek (1989b), Absolute differential and integral electron excitation cross sections for atomic oxygen: VIII. The $^3P-^5S^0$ transition (1356 Å) from 13.9 to 30 eV, *J. Geophys. Res.*, *94*, 2733–2736, doi:10.1029/JA094iA03p02733.
- Dols, V. J., F. Bagenal, T. A. Cassidy, F. J. Cray, and P. A. Delamere (2015), Europa's atmospheric neutral escape: Importance of symmetrical O_2 charge exchange, *Icarus*, *264*, 387–397.
- Eviatar, A., D. F. Strobel, B. C. Wolven, P. D. Feldman, M. A. McGrath, and D. J. Williams (2001), Excitation of the Ganymede ultraviolet aurora, *Astrophys. J.*, *555*, 1013–1019, doi:10.1086/321510.
- Famá, M., J. Shi, and R. A. Baragiola (2008), Sputtering of ice by low-energy ions, *Surf. Sci.*, *602*, 156–161, doi:10.1016/j.susc.2007.10.002.
- Feldman, P. D., M. A. McGrath, D. F. Strobel, H. W. Moos, K. D. Retherford, and B. C. Wolven (2000), HST/STIS ultraviolet imaging of polar aurora on Ganymede, *Astrophys. J.*, *535*, 1085–1090, doi:10.1086/308889.
- Geissler, P. E., W. H. Smyth, A. S. McEwen, W. Ip, M. J. S. Belton, T. V. Johnson, A. P. Ingersoll, K. Rages, W. Hubbard, and A. J. Dessler (2001), Morphology and time variability of Io's visible aurora, *J. Geophys. Res.*, *106*, 26,137–26,146, doi:10.1029/2000JA002511.
- Greeley, R., C. F. Chyba, I. J. W. Head, T. B. McCord, W. B. McKinnon, R. T. Pappalardo, and P. H. Figueredo (2004), Geology of Europa, in *Jupiter: The Planet, Satellites and Magnetosphere*, edited by R. Greeley et al., pp. 329–362, Cambridge Univ. Press, Cambridge, U. K.
- Hall, D. T., D. F. Strobel, P. D. Feldman, M. A. McGrath, and H. A. Weaver (1995), Detection of an oxygen atmosphere on Jupiter's moon Europa, *Nature*, *373*(6516), 677–679.
- Hall, D. T., P. D. Feldman, M. A. McGrath, and D. F. Strobel (1998), The far-ultraviolet oxygen airglow of Europa and Ganymede, *Astrophys. J.*, *499*(5), 475–481.
- Hansen, C. J., D. E. Shemansky, and A. R. Hendrix (2005), Cassini UVIS observations of Europa's oxygen atmosphere and torus, *Icarus*, *176*(2), 305–315.
- Hess, S. L. G., B. Bonfond, P. Zarka, and D. Grodent (2011), Model of the Jovian magnetic field topology constrained by the Io auroral emissions, *J. Geophys. Res.*, *116*, A05217, doi:10.1029/2010JA016262.
- Hill, T. W., and F. C. Michel (1976), Heavy ions from the Galilean satellites and the centrifugal distortion of the Jovian magnetosphere, *J. Geophys. Res.*, *81*, 4561–4565, doi:10.1029/JA081i025p04561.
- Hill, T. W., A. J. Dessler, and F. C. Michel (1974), Configuration of the Jovian magnetosphere, *Geophys. Res. Lett.*, *1*, 3–6, doi:10.1029/GL001i001p00003.
- Johnson, R. E., L. J. Lanzerotti, and W. L. Brown (1982), Planetary applications of ion induced erosion of condensed-gas frosts, *Nucl. Instrum. Methods*, *198*, 147–157, doi:10.1016/0167-5087(82)90066-7.
- Johnson, R. E., R. W. Carlson, J. F. Cooper, C. Paranicas, M. H. Moore, and M. C. Wong (2004), Radiation effects on the surfaces of the Galilean satellites, in *Jupiter: The Planet, Satellites and Magnetosphere*, edited by R. E. Johnson et al., pp. 485–512, Cambridge Univ. Press, Cambridge, U. K.
- Johnson, R. E., M. H. Burger, T. A. Cassidy, F. Leblanc, M. Marconi, and W. H. Smyth (2009), Composition and detection of Europa's sputter-induced atmosphere, in *Europa*, edited by R. E. Johnson et al., pp. 507–527, Univ. of Arizona Press, Tucson.
- Kanik, I., C. Noren, O. P. Makarov, P. Vatti Palle, J. M. Ajello, and D. E. Shemansky (2003), Electron impact dissociative excitation of O_2 : 2. Absolute emission cross sections of the OI(130.4 nm) and OI(135.6 nm) lines, *J. Geophys. Res.*, *108*, 5126, doi:10.1029/2000JE001423.
- Khurana, K. K., M. G. Kivelson, D. J. Stevenson, G. Schubert, C. T. Russell, R. J. Walker, and C. Polanskey (1998), Induced magnetic fields as evidence for subsurface oceans in Europa and Callisto, *Nature*, *395*, 777–780, doi:10.1038/27394.
- Khurana, K. K., M. G. Kivelson, V. M. Vasylunas, N. Krupp, J. Woch, A. Lagg, B. H. Mauk, and W. S. Kurth (2004), The configuration of Jupiter's magnetosphere, in *Jupiter: The Planet, Satellites and Magnetosphere*, edited by K. K. Khurana et al., pp. 593–616, Cambridge Univ. Press, Cambridge, U. K.
- Kivelson, M. G., F. Bagenal, W. S. Kurth, F. M. Neubauer, C. Paranicas, and J. Saur (2004), Magnetospheric interactions with satellites, in *Jupiter: The Planet, Satellites and Magnetosphere*, edited by F. Bagenal, T. E. Dowling, and W. B. McKinnon, chap. 21, pp. 513–536, Cambridge Univ. Press, Cambridge, U. K.
- Kliore, A. J., D. P. Hinson, F. M. Flasar, A. F. Nagy, and T. E. Cravens (1997), The ionosphere of Europa from Galileo radio occultations, *Science*, *277*(5324), 355–358.
- Krist, J. E., R. N. Hook, and F. Stoehr (2011), 20 years of Hubble Space Telescope optical modeling using Tiny Tim, in *Society of Photo-Optical Instrumentation Engineers (SPIE) Conference Series*, vol. 8127, pp. 1–16, doi:10.1117/12.892762.
- Kurth, W. S., D. A. Gurnett, A. M. Persoon, A. Roux, S. J. Bolton, and C. J. Alexander (2001), The plasma wave environment of Europa, *Planet. Space Sci.*, *49*, 345–363.
- Lagg, A., N. Krupp, J. Woch, and D. J. Williams (2003), In-situ observations of a neutral gas torus at Europa, *Geophys. Res. Lett.*, *30*(11), 1556, doi:10.1029/2003GL017214.
- Mauk, B. H., D. G. Mitchell, S. M. Krimigis, E. C. Roelof, and C. P. Paranicas (2003), Energetic neutral atoms from a trans-Europa gas torus at Jupiter, *Nature*, *421*, 920–922.
- McGrath, M. A., E. Lellouch, D. F. Strobel, P. D. Feldman, and R. E. Johnson (2004), Satellite atmospheres, in *Jupiter: The Planet, Satellites and Magnetosphere*, edited by M. A. McGrath pp. 457–483, Cambridge Univ. Press, Cambridge, U. K.
- McGrath, M. A., C. J. Hansen, and A. R. Hendrix (2009), Observations of Europa's tenuous atmosphere, in *Europa*, edited by M. A. McGrath, C. J. Hansen, and A. R. Hendrix, pp. 485–505, Univ. of Arizona Press, Tucson, Arizona.
- McGrath, M. A., X. Jia, K. Retherford, P. D. Feldman, D. F. Strobel, and J. Saur (2013), Aurora on Ganymede, *J. Geophys. Res. Space Physics*, *118*, 2043–2054, doi:10.1002/jgra.50122.
- Meyer-Vernet, N., M. Moncuquet, and S. Hoang (1995), Temperature inversion in the Io plasma torus, *Icarus*, *116*, 202–213, doi:10.1006/icar.1995.1121.
- Neubauer, F. M. (1998), The sub-Alfvénic interaction of the Galilean satellites with the Jovian magnetosphere, *J. Geophys. Res.*, *103*(E9), 19,843–19,866.
- Oliverson, R. J., F. Scherb, W. H. Smyth, M. E. Freed, R. C. J. Woodward, M. L. Marconi, K. D. Retherford, O. L. Lupie, and J. P. Morgenthaler (2001), Sunlit Io atmospheric [OI] 6300 Å emission and the plasma torus, *J. Geophys. Res.*, *106*, 26,183–26,194, doi:10.1029/2000JA002507.
- Plainaki, C., A. Milillo, A. Mura, J. Saur, S. Orsini, and S. Massetti (2013), Exospheric O_2 densities at Europa during different orbital phases, *Planet. Space Sci.*, *88*, 42–52, doi:10.1016/j.pss.2013.08.011.

- Rathbun, J. A., N. J. Rodriguez, and J. R. Spencer (2010), Galileo PPR observations of Europa: Hotspot detection limits and surface thermal properties, *Icarus*, 210, 763–769, doi:10.1016/j.icarus.2010.07.017.
- Retherford, K. D., H. W. Moos, D. F. Strobel, B. C. Wolven, and F. L. Roesler (2000), Io's equatorial spots: Morphology of neutral UV emissions, *J. Geophys. Res.*, 105, 27,157–27,166, doi:10.1029/2000JA002500.
- Retherford, K. D., H. W. Moos, and D. F. Strobel (2003), Io's auroral limb glow: Hubble Space Telescope FUV observations, *J. Geophys. Res.*, 108, 1333–1341, doi:10.1029/2002JA009710.
- Retherford, K. D., et al. (2007), Icy Galilean satellite UV observations by new horizons and HST, *Eos Trans. AGU*, 88(52), Fall Meet. Suppl., Abstract P53C–06.
- Roesler, F. L., H. W. Moos, R. J. Oliverson, R. C. Woodward, K. D. Retherford, F. Scherb, M. A. McGrath, W. H. Smyth, P. D. Feldman, and D. F. Strobel (1999), Far-ultraviolet imaging spectroscopy of Io's atmosphere with HST/STIS, *Science*, 283(5400), 353–357.
- Roth, L., J. Saur, K. D. Retherford, D. F. Strobel, P. D. Feldman, M. A. McGrath, and F. Nimmo (2014a), Transient water vapor at Europa's south pole, *Science*, 343, 171–174, doi:10.1126/science.1247051.
- Roth, L., K. D. Retherford, J. Saur, D. F. Strobel, P. D. Feldman, M. A. McGrath, and F. Nimmo (2014b), Orbital apocenter is not a sufficient condition for HST/STIS detection of Europa's water vapor aurora, *Proc. Natl. Acad. Sci.*, 111(48), E5123–E5132.
- Roth, L., J. Saur, K. D. Retherford, P. D. Feldman, and D. F. Strobel (2014c), A phenomenological model of Io's UV aurora based on HST/STIS observations, *Icarus*, 228, 386–406, doi:10.1016/j.icarus.2013.10.009.
- Rubin, M., et al. (2015), Self-consistent multifluid MHD simulations of Europa's exospheric interaction with Jupiter's magnetosphere, *J. Geophys. Res. Space Physics*, 120, 3503–3524, doi:10.1002/2015JA021149.
- Saur, J., and D. F. Strobel (2004), Relative contributions of sublimation and volcanoes to Io's atmosphere inferred from its plasma interaction during solar eclipse, *Icarus*, 171, 411–420, doi:10.1016/j.icarus.2004.05.010.
- Saur, J., D. F. Strobel, and F. M. Neubauer (1998), Interaction of the Jovian magnetosphere with Europa: Constraints on the neutral atmosphere, *J. Geophys. Res.*, 103(E9), 19,947–19,962.
- Saur, J., F. M. Neubauer, D. F. Strobel, and M. E. Summers (1999), Three-dimensional plasma simulation of Io's interaction with the Io plasma torus: Asymmetric plasma flow, *J. Geophys. Res.*, 104, 25,105–25,126, doi:10.1029/1999JA900304.
- Saur, J., F. M. Neubauer, D. F. Strobel, and M. E. Summers (2000), Io's ultraviolet aurora: Remote sensing of Io's interaction, *Geophys. Res. Lett.*, 27, 2893–2896.
- Saur, J., P. D. Feldman, L. Roth, F. Nimmo, D. F. Strobel, K. D. Retherford, M. A. McGrath, N. Schilling, J.-C. Gérard, and D. Grodent (2011), Hubble space telescope/advanced camera for surveys observations of Europa's atmospheric ultraviolet emission at eastern elongation, *Astrophys. J.*, 738, 153, doi:10.1088/0004-637X/738/2/153.
- Saur, J., T. Grambusch, S. Duling, F. M. Neubauer, and S. Simon (2013), Magnetic energy fluxes in sub-Alfvénic planet star and moon planet interactions, *Astron. Astrophys.*, 552, A119, doi:10.1051/0004-6361/201118179.
- Saur, J., et al. (2015), The search for a subsurface ocean in Ganymede with Hubble Space Telescope observations of its auroral ovals, *J. Geophys. Res. Space Physics*, 120, 1715–1737, doi:10.1002/2014JA020778.
- Schilling, N., F. M. Neubauer, and J. Saur (2007), Time-varying interaction of Europa with the Jovian magnetosphere: Constraints on the conductivity of Europa's subsurface ocean, *Icarus*, 192, 41–55.
- Schilling, N., F. M. Neubauer, and J. Saur (2008), Influence of the internally induced magnetic field on the plasma interaction of Europa, *J. Geophys. Res. Space Physics*, 113, A03203, doi:10.1029/2007JA012842.
- Schmidt, B. E., D. D. Blankenship, G. W. Patterson, and P. M. Schenk (2011), Active formation of 'chaos terrain' over shallow subsurface water on Europa, *Nature*, 479, 502–505, doi:10.1038/nature10608.
- Schneider, N. M., and F. Bagenal (2007), Io's neutral clouds, plasma torus, and magnetospheric interaction, in *Io After Galileo: A New View of Jupiter's Volcanic Moon*, edited by N. M. Schneider and F. Bagenal, pp. 265, Springer, Berlin.
- Shemansky, D. E., Y. L. Yung, X. Liu, J. Yoshii, C. J. Hansen, A. R. Hendrix, and L. W. Esposito (2014), A new understanding of the Europa atmosphere and limits on geophysical activity, *Astrophys. J.*, 797, 84, doi:10.1088/0004-637X/797/2/84.
- Shematovich, V. I., R. E. Johnson, J. F. Cooper, and M. C. Wong (2005), Surface-bounded atmosphere of Europa, *Icarus*, 173, 480–498, doi:10.1016/j.icarus.2004.08.013.
- Sittler, E. C., and D. F. Strobel (1987), Io plasma torus electrons: Voyager 1, *J. Geophys. Res.*, 92, 5741–5762, doi:10.1029/JA092iA06p05741.
- Smyth, W. H., and M. L. Marconi (2006), Europa's atmosphere, gas tori, and magnetospheric implications, *Icarus*, 181, 510–526, doi:10.1016/j.icarus.2005.10.019.
- Smyth, W. H., C. A. Peterson, and M. L. Marconi (2011), A consistent understanding of the ribbon structure for the Io plasma torus at the Voyager 1, 1991 ground-based, and Galileo J0 epochs, *J. Geophys. Res.*, 116, A07205, doi:10.1029/2010JA016094.
- Spencer, J. R., L. K. Tamppari, T. Z. Martin, and L. D. Travis (1999), Temperatures on Europa from Galileo photopolarimeter-radiometer: Nighttime thermal anomalies, *Science*, 284, 1514–1516, doi:10.1126/science.284.5419.1514.
- Wannawichian, S., J. T. Clarke, and J. D. Nichols (2010), Ten years of Hubble Space Telescope observations of the variation of the Jovian satellites' auroral footprint brightness, *J. Geophys. Res.*, 115, A02206, doi:10.1029/2009JA014456.
- Woods, T. N., et al. (1996), Validation of the UARS solar ultraviolet irradiances: Comparison with the ATLAS 1 and 2 measurements, *J. Geophys. Res.*, 101, 9541–9570, doi:10.1029/96JD00225.
- Woods, T. N., F. G. Eparvier, S. M. Bailey, P. C. Chamberlin, J. Lean, G. J. Rottman, S. C. Solomon, W. K. Tobiska, and D. L. Woodraska (2005), Solar EUV Experiment (SEE): Mission overview and first results, *J. Geophys. Res.*, 110(A9), A01312, doi:10.1029/2004JA010765.
- Zimmer, C., K. K. Khurana, and M. G. Kivelson (2000), Subsurface oceans on Europa and Callisto: Constraints from Galileo magnetometer observations, *Icarus*, 147, 329–347, doi:10.1006/icar.2000.6456.